

Banner appropriate to article type will appear here in typeset article

Heavy Kolmogorov-size spheres suppress the inertial cascade in homogeneous and isotropic turbulence

Ludovico Fossà¹ and Marco Edoardo Rosti¹¹Complex Fluids and Flows Unit, Okinawa Institute of Science and Technology, 1919-1 Tancha, Onna-son, Kunigami-gun, Okinawa-ken 904-0495 Japan**Corresponding author:** Marco Edoardo Rosti marco-rosti@oist.jp

(Received xx; revised xx; accepted xx)

The effect of Kolmogorov-size spherical particles on homogeneous and isotropic turbulence is investigated using particle-resolved direct numerical simulations at a Taylor-scale Reynolds number of 150. Four monodisperse suspensions of particles with identical diameter and volume fraction 10^{-3} are considered, while the particle-to-fluid density ratio varies between 100 and 1500 and the mass fraction between 0.1 and 0.6. As particle inertia increases, the energy spectrum departs from the canonical Kolmogorov $\kappa^{-5/3}$ scaling and approaches a peculiar regime with κ^{-1} . In this limit, the nonlinear energy transfer is strongly suppressed and the kinetic energy balance is dominated by the fluid-solid interaction and the viscous dissipation. Consistently, the second-order structure function shows logarithmic scaling at separations larger than the particle diameter, indicating velocity decorrelation. Increasing particle inertia promotes axial strain and vortex compression in the vicinity of the particles and enhances the particle-fluid relative velocity. Particle clustering weakens as the density ratio and the Stokes number increase, with the volume and the population of the clusters decreasing when inertia is enhanced. Nevertheless, when clustering occurs, particles preferentially sample regions of high strain and low vorticity, for all the values of the density ratio and the mass fraction considered here.

Key words:

1. Introduction

Particle-laden flows are ubiquitous in nature and engineering (Brandt & Coletti 2022; Marchioli *et al.* 2025, 2026). Examples include cloud droplets and volcanic ashes in planetary atmospheres (Mellado 2017; Rose & Durant 2009), the formation of protoplanetary disks (Birnstiel 2024), the dispersal of phytoplankton and microplastics in the ocean (Borgnino *et al.* 2019; Sugathapala *et al.* 2025), the transport of blood cells (Freund 2014) and industrial processes such as flue gas scrubbing (Lee *et al.* 2013) and fuel atomization in spray combustion (Jenny *et al.* 2012). These phenomena see a turbulent carrier flow

transporting and interacting with a solid (or liquid) suspension, with the latter phase that can either energise or weaken its motion. The nature of this modulation depends on factors such as the relative size of the particle and the turbulent eddies, the inertia of the suspension and the degree of dilution of the suspension (Gore & Crowe 1989; Balachandar & Eaton 2010; Brandt & Coletti 2022). In particular, the dispersed phase does not exert a direct mechanical forcing on the carrier flow when it is highly diluted, its inertia is moderate and the particle size is much smaller than the smallest scale of the turbulent motion (Brandt & Coletti 2022).

Dilute suspensions are characterised by a small volume fraction $\Phi_p = V_p/(V_f + V_p) \leq 10^{-3}$, where V_f and V_p are the volume occupied by the fluid and dispersed phase, respectively, and by a small inertia of a suspension, described by the density ratio $\Psi_p = \rho_p/\rho_f$, ρ_p and ρ_f being the volume density of the dispersed particles and the carrier fluid, respectively (Balachandar & Eaton 2010). In general, particles with a size D much smaller than the Kolmogorov length scale η are assumed to not exert a significant backreaction on the carrier flow. They are mostly swayed by the local fluid motion, with the intensity of their response being mediated by their own inertia. Particles of negligible inertia behave as pure tracers and follow the motion of the carrier flow, while particles of large inertia are only weakly affected by the surface stresses induced by the carrier flow and do not follow its streamlines. Particles of moderate inertia are expected to be only partially influenced by the carrier flow, their trajectory departing from its streamlines in the presence of intense velocity gradients. This centrifugal mechanism was proposed by Maxey (1987), who showed that small, light spherical particles segregate in regions of low vorticity and high strain, and that this behaviour intensifies for increasing particle mass. His predictions were later confirmed numerically by Squires & Eaton (1990). This preferential sampling of the flow has been indicated as a key process in the formation and evolution of clusters in homogeneous and isotropic turbulence (see the reviews of Balachandar & Eaton 2010 and Brandt & Coletti 2022). The sweep-stick mechanism of Goto & Vassilicos (2008) has also been proposed to account for preferential sampling in flows laden with smaller-than-Kolmogorov and finite-size particles (Yoshimoto & Goto 2007; Uhlmann & Chouippe 2017).

When forming dilute suspensions, light, smaller-than-Kolmogorov particles behave essentially as passive tracers of a one-way coupled mechanical system (Sumbekova *et al.* 2017). These flows have been extensively investigated with the aid of point-particle direct numerical simulations (DNSs) where the motion of each particle is governed by a Lagrangian tracker (Maxey & Riley 1983; Matsuda *et al.* 2024). Point-particle DNSs rely on the assumption of uniform flow properties across larger-than-particle distances $D/\eta \ll 1$, meaning that the sub-Kolmogorov scales need not be resolved (Brandt & Coletti 2022). Although enormous efforts have been made in the development of two-way coupling models (Balachandar *et al.* 2019), point-particle DNSs are yet to provide an accurate and complete description of the particle-fluid interaction when $D/\eta = O(1)$, a condition typical of several practical scenarios in which the dispersed phase modulates the turbulence (Luo *et al.* 2017; Tanaka & Eaton 2010; Oka & Goto 2022). In recent years, particle-resolved direct numerical simulations (PR-DNSs) based on the immersed boundary method (IBM) have cast new light on the interphase coupling in suspensions of larger-than-Kolmogorov ($D/\eta \gg 1$) spherical particles (Kajishima *et al.* 2001; Uhlmann 2005; Breugem 2012; Kempe & Fröhlich 2012; Hori *et al.* 2022). To name a few, we recall the works by Lucci *et al.* (2010), Uhlmann & Chouippe (2017), Chouippe & Uhlmann (2019), Oka & Goto (2022), Olivieri *et al.* (2022a), Chiarini & Rosti (2024) and Cannon *et al.* (2024) for homogeneous isotropic turbulence, and those by Uhlmann (2008), Ardekani & Brandt

(2019), Rosti & Brandt (2020), Costa *et al.* (2021) and Gao *et al.* (2023) for turbulent channel flows. These works highlight the importance of the ratio D/η on turbulence modulation: inertial-scale particles provide a spectral shortcut by extracting energy from the large scales and reinjecting it into the small ones (Lucci *et al.* 2010; Oka & Goto 2022; Chiarini & Rosti 2024), whereas Kolmogorov-size particles absorb the carrier flow's kinetic energy (Tanaka & Eaton 2010) and may impose a decay rate of the energy spectrum proportional to the inverse fourth power of their spatial wavenumber (Chiarini *et al.* 2025).

Small, heavy particles can attenuate the turbulent fluctuations just like large, light ones (Oka & Goto 2022). Along with the volume fraction Φ_p and the size ratio D/η , the particle-to-fluid density ratio $\Psi_p = \rho_p/\rho_f$ plays a key role on the interphase coupling (Brandt & Coletti 2022). Yu *et al.* (2017) performed PR-DNSs with a direct forcing-fictitious domain method to study the effect of increasing Ψ_p in the range $1 - 100$ on a turbulent channel flow at a friction Reynolds number $Re_\tau = 180$ and volume fraction $\Phi_p = 8.4 \times 10^{-3}$. They considered two sets of spherical particles of diameter 0.1 and 0.2 times the channel half-width, which corresponds to $D/\eta \approx 5$ and $D/\eta \approx 10$, respectively. They reported a non-monotonical trend of the total drag, which first increased along with the viscous dissipation for $\Psi_p \leq 10$, but diminished as the formation of near-wall streamwise vortices was inhibited (Lucci *et al.* 2010). Tavanashad *et al.* (2019) investigated non-dilute populations of larger-than-Kolmogorov spherical particles by performing PR-DNSs on a triperiodic box. They considered several orders of magnitude of Ψ_p ($10^{-3} - 10^3$) and showed that heavier suspensions extract more kinetic energy from the carrier flow. Although they did not report the Kolmogorov length scale nor the Reynolds number considered in their simulations, they used two sets of particles with diameter 20 and 30 times larger than the grid cell. More recently, Shen *et al.* (2024) performed PR-DNSs using a lattice-Boltzmann method to study the effect of variable particle density on finite-size spherical particles on a turbulent channel flow, with particles in the range $6 \lesssim D/\eta \lesssim 23$. Two-way coupled point-particle DNSs have also been employed to study the effect of particle inertia in suspensions of smaller-than-Kolmogorov spherical particles. Mortimer & Fairweather (2020) studied the effect of increasing Ψ_p on near-wall coherent structures in a channel flow laden with 300 000 spheres at a friction Reynolds number $Re_\tau = 180$ and volume fraction $\Phi_p = 10^{-4}$. Their results showed a monotonical attenuation of the turbulent fluctuations in the near-wall region with increasing particle density. Gualtieri *et al.* (2023) conducted an extensive simulation campaign of non-dilute suspensions ($\Phi_p = 0.4$) of smaller-than-Kolmogorov spheres in channel flows and concluded that dense particles deplete a considerable amount of turbulent kinetic energy. Consistently with the results of Yu *et al.* (2017), they reported an increase in friction drag in the presence of light particles, which acted as a source of turbulent kinetic energy near the wall.

A broad body of work has focused on particles either much smaller ($D/\eta \ll 1$) or much larger ($D/\eta \gg 1$) than the Kolmogorov scale, while particles of Kolmogorov size have received far less attention. This is largely due to the extreme spatial resolution required to characterise the fluid field at the sub-particle scale. Among the experimental studies in homogeneous and isotropic turbulence, we recall Hwang & Eaton (2006), who investigated the sedimentation of glass spheres with $\Psi_p \approx 2500$, Poelma *et al.* (2007), who examined the effect of heavy particles on the decay of grid-generated turbulence, and Tanaka & Eaton (2010), who performed high-resolution particle image velocimetry. They concluded that particles with a smaller diameter and a higher density induce the strongest attenuation in steady-state homogeneous and isotropic turbulence. Numerical simulations permit us to investigate isotropic flows in the absence of gravity. However, resolving the sub-particle motion via PR-DNSs requires grid spacings well below η , thus rendering the computational

cost prohibitive even at moderate Reynolds numbers. Using the IBM proposed by Uhlmann (2005), Uhlmann & Chouippe (2017) were able to investigate a particle laden triperiodic flow at $Re_\lambda \cong 115$ and with $D/\eta = 5$, slightly above the Kolmogorov scale. Schneiders *et al.* (2017) conducted PR-DNSs of a triperiodic turbulent flow laden Kolmogorov-size spheres with $D/\eta \cong 1.32$ using a Cartesian cut-cell method. They considered a suspension of 45 000 particles in a decaying homogeneous and isotropic turbulent flow and density ratios Ψ_p in the range 40 – 5000. The enormous computational burden entailed by the resolution of sub-Kolmogorov motions limited the initial value of the Taylor-based Reynolds number to 70. Chiarini *et al.* (2025) used the IBM of Hori *et al.* (2022) to characterise the behavior of a suspension of particles with diameter $D \cong \eta$ and $\Psi_p = 5, 100$. They compared their results with those obtained from point-particle simulations and reported significant discrepancies for the cases with the highest density ratio.

1.1. Objectives and outline

In this work, we examine how increasing particle inertia modulates homogeneous and isotropic turbulence laden with Kolmogorov-scale spherical particles ($D = \eta$). The primary objective is to quantify the impact of small, dense particles on the turbulent cascade, the scale-by-scale energy transfer, and the small-scale intermittency of the carrier flow, as well as to assess how increasing particle inertia shapes the collective dynamics of the disperse phase and the structure of particle clusters. To this end, we perform large-scale particle-resolved direct numerical simulations of a homogeneous, isotropic, triply periodic turbulent flow. A Taylor-scale Reynolds number of $Re_\lambda \cong 150$ is selected to ensure adequate scale separation within the inertial subrange in the unladen case. We consider a fixed particle volume fraction $\Phi_p = 10^{-3}$ and density ratios up to $\Psi_p = 1500$, a regime that lies beyond the range of validity of point-particle approaches and is directly relevant to natural and industrial flows (Brandt & Coletti 2022; Marchioli *et al.* 2025).

The paper is organised as follows. The numerical method and its implementation are described in §2, and the post-processing procedures and results are presented in §3. In particular, the bulk statistics of the carrier flow are discussed in §3.1, followed by energy spectra and structure functions in §3.2, the scale-by-scale energy budget in §3.3, and the analysis of the velocity-gradient tensor in §3.4. Particle dynamics and clustering statistics are examined in §3.5 and §3.6, respectively, while the particles' preferential sampling is discussed in §3.7. Finally, conclusions are drawn in §4.

2. Direct numerical simulations

We consider a triply periodic cubic domain of volume L^3 , where L is the side length of the cube. The carrier flow (fluid phase) is governed by the incompressible Navier-Stokes equations for momentum conservation and the continuity constraint:

$$\frac{\partial u_i}{\partial t} + \frac{\partial u_j u_i}{\partial x_j} = \frac{1}{\rho_f} \frac{\partial \sigma_{ij}}{\partial x_j} + f_i^{\text{ABC}} + f_i^{\text{part}}, \quad (2.1a)$$

$$\frac{\partial u_k}{\partial x_k} = 0, \quad (2.1b)$$

where Einstein summation over repeated indices is implied. Here, u_i is the fluid velocity, ρ_f the fluid density, and f_i^{part} is the IBM forcing exerted by the solid particles on the fluid (Hori *et al.* 2022). The large-scale volume forcing f_i^{ABC} is of the Arnold-Beltrami-Childress (ABC) type (Arnold 1965, p. 20)

$$f_x^{\text{ABC}} = F_0 \left[\cos \left(\frac{2\pi}{L} y \right) + \sin \left(\frac{2\pi}{L} z \right) \right], \quad (2.2a)$$

$$f_y^{\text{ABC}} = F_0 \left[\cos \left(\frac{2\pi}{L} z \right) + \sin \left(\frac{2\pi}{L} x \right) \right], \quad (2.2b)$$

$$f_z^{\text{ABC}} = F_0 \left[\cos \left(\frac{2\pi}{L} x \right) + \sin \left(\frac{2\pi}{L} y \right) \right]. \quad (2.2c)$$

Because the carrier flow is Newtonian and incompressible, the stress tensor σ_{ij} reads

$$\sigma_{ij} = -p\delta_{ij} + 2\mu_f S_{ij}, \quad (2.3)$$

where p is the fluid pressure, δ_{ij} is the Kronecker delta, μ_f is the dynamic viscosity and $S_{ij} = (\partial_j u_i + \partial_i u_j)/2$ is the symmetric part of the velocity gradient tensor $\partial_j u_i$. From this point onwards, the kinematic viscosity of the fluid phase $\nu_f = \mu_f/\rho_f$ will be used.

The velocity of a point inside a solid spherical particle is due to the contribution of the translational velocity and the rotation around the particle center $U_i = \tilde{U}_i + \epsilon_{ijk} \Omega_j r_k$, where Ω_j is the particle rotational velocity, ϵ_{ijk} the Levi-Civita tensor, and r_k the radial distance from the particle center. The time evolution of \tilde{U}_i and Ω_i is governed by the Newton-Euler equations for the translational velocity \tilde{U}_i and the angular velocity Ω_j

$$m_p \frac{d\tilde{U}_i}{dt} = \oint_{\partial V_p} \sigma_{ij} n_j d(\partial V) + F_i^{\text{col}}, \quad (2.4a)$$

$$\mathcal{I}_p \frac{d\Omega_i}{dt} = \oint_{\partial V_p} \epsilon_{ijk} r_j \sigma_{kl} n_l d(\partial V). \quad (2.4b)$$

Here, F^{col} is the force exerted by inter-particle collisions, σ_{ij} is defined in (2.3), n_i is outer normal to the particle surface, $m_p = (\pi/6)\rho_p D^3$ and $\mathcal{I}_p = (m_p/10)D^2$ are the particle mass and moment of inertia, respectively, and D is the particle diameter. No-slip and no-penetration conditions are applied at the particle surface $u_i = U_i$, where the velocity of the fluid and solid phase match. The particle translational velocity is integrated at every time step to update the particle location X_i , where $\tilde{U}_i = dX_i/dt$. Inter-particle collisions are handled with the mass-spring-dash pot model of Tsuji *et al.* (1993) and Costa *et al.* (2015). A repulsive force acts on the particles as soon as their volumes overlap, i.e. when the distance of their centres falls below D .

We consider a monodisperse (i.e. uniform in size) population of $N = 74\,208$ spherical particles with diameter $D \cong 0.003L$ that matches the Kolmogorov scale η in all the cases examined. The volume fraction of the solid phase is kept constant $\Phi_p = (\pi N/6)(D/L)^3 = 10^{-3}$ across all simulations. Thus, the mass fraction is determined solely by the density ratio $\Psi_p = \rho_p/\rho_f$ through the relation

$$M_p = \frac{\Psi_p \Phi_p}{1 - \Phi_p + \Psi_p \Phi_p}. \quad (2.5)$$

Four laden cases with density ratio $\Psi_p = 100, 250, 666, 1499$ and mass fraction $M_p = 0.1, 0.2, 0.4, 0.6$ are considered and compared to the unladen case ($\Phi_p = M_p = 0$). These values of M_p match those used in the experiments of Tanaka & Eaton (2010) (see table 3 therein).

The numerical method described in this section is implemented on the in-house Fortran code [Fujin](#). The momentum equation for the fluid phase (2.1a) is advanced in time with a fractional step method (Amsden & Harlow 1970; Kim *et al.* 1987; Tomé *et al.* 1996). The nonlinear and viscous terms in (2.1a) are discretised using an Adams-Bashforth scheme in

the predictor step, while incompressibility is enforced by solving the Poisson equation for the pressure with a fast Fourier transform. The interplay of the fluid phase and the solid spheres is taken into account with the Eulerian IBM described by Hori *et al.* (2022). A fixed-radius, near-neighbours search algorithm is used to reduce the computational cost of the collisions from $O(N^2)$ to $O(N)$ (Monti *et al.* 2021). The code uses a two-dimensional Cartesian parallelisation provided by the Message-Passage Interface (MPI) library. The triperiodic cubic domain is discretized using an uniform cartesian grid of 2048^3 points and all the computations were performed using 4096 cores on the CPU-based cluster [Deigo](#) at the Okinawa Institute for Science and Technology.

3. Postprocessing and results

We present and discuss the results of the PR-DNSs performed using the method described in §2. Since the volume fraction is fixed, each density ratio corresponds to a unique mass fraction through (2.5). For clarity, the laden cases are therefore identified by their mass fraction M_p .

3.1. Bulk statistics of the carrier flow

Increasing the inertia of Kolmogorov-size particles has a dramatic effect on the large-scale dynamics of the turbulent carrier flow. The four panels in figure 1 show the effect of M_p (and Ψ_p) on the dissipation rate $\varepsilon = 2\nu_f S_{ij} S_{ij}$, where S_{ij} is the symmetric part of the velocity gradient tensor defined in §2. The color scale is logarithmic and ranges between 1 (dark blue) and 10^4 (dark orange), with the particles' location marked by the localized spots of high dissipation associated to the shear layers at the particles' surface (Cannon *et al.* 2024). All the cases show large excursions in ε . Adding the suspension with the lowest mass fraction ($M_p = 0.1$, figure 1a) results in a flow field which features large regions of high dissipation (yellow and orange) and low dissipation (dark blue), with the particles residing mostly in the former and avoiding the latter. These contiguous regions break down into smaller ones and the peaks of large ε become confined to the particles' shear layers as M_p increases to 0.2 (b) and 0.4 (c). When $M_p = 0.6$ (d), the large regions of high ε vanish: the flow field is characterised by smaller, adjacent regions of moderate (yellow) and low (blue) ε , while the dissipation remains still elevated in the particles' wakes. As can be observed in figure 2, increasing the particle inertia has a similar effect on the enstrophy $\mathcal{E} = \omega_i \omega_i / 2$, where $\omega_i = -\epsilon_{ijk} W_{jk}$ is the vorticity and $W_{ij} = (\partial_j u_i - \partial_i u_j) / 2$ is the skew-symmetric part of the velocity gradient tensor $\partial_j u_i$ (Meneveau 2011; Davidson 2015). Similarly to the dissipation, these large regions of intense vorticity disappear as M_p increases, and high values of the enstrophy remain confined to the particles' wakes. As shown in the insets of figures 1a, d and of figures 2a and d, elongated laminar wakes appear as M_p increases and the carrier flow becomes more intermittent at the particle scale.

Figures 1 and 2 suggest that the broad range of spatial scales and the direct energy cascade typical of homogeneous and isotropic turbulent flows disappear as the density of the particles increases. To gain further insights on the effect of the particle inertia on the physical properties of the carrier flow, which are point-wise quantities local in space and time, we compute their spatial and temporal averages. Their values (denoted with the operator $\langle \cdot \rangle$) are made non-dimensional and listed in table 1. Here, the four laden cases shown in the visualizations 1 and 2 are compared with the unladen case $M_p = 0$. The kinetic energy is $K = u_i u_i / 2$, the dissipation rate was defined earlier in this section as $\varepsilon = 2\nu_f S_{ij} S_{ij}$, the Kolmogorov length scale is $\eta = (\nu_f^3 / \varepsilon)^{1/4}$ the Kolmogorov time scale is $(\nu_f / \varepsilon)^{1/2}$, the longitudinal Taylor length scale is $\lambda = (20\nu_f K / \varepsilon)^{1/2}$ and the Taylor-based

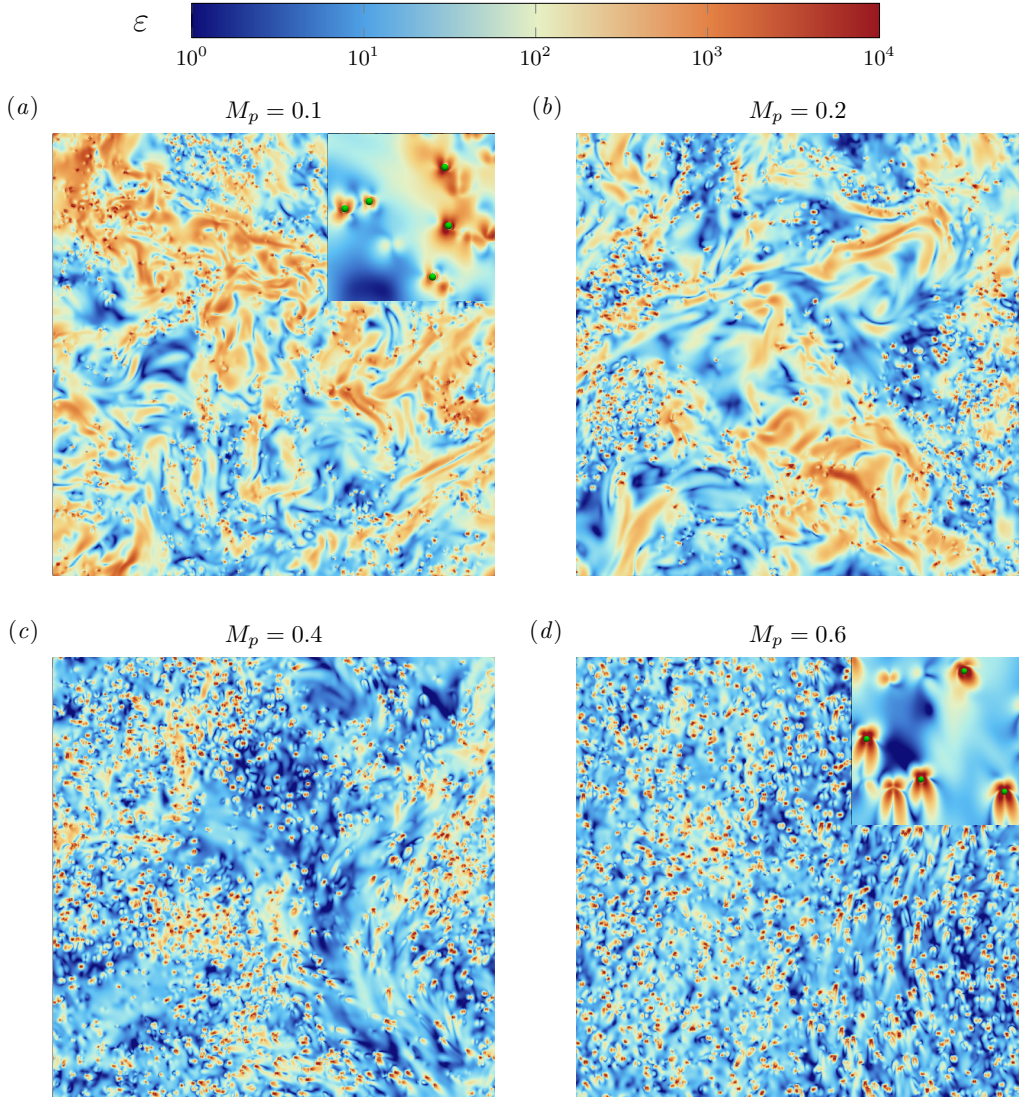


Figure 1. Effect of increasing particle-to-fluid density ratio and mass fraction on the turbulent dissipation rate, ε . Each panel shows the dissipation rate with a logarithmic color scale in a particle-laden domain with different mass fractions: $M_p = 0.1$ (a), 0.2 (b), 0.4 (c), and 0.6 (d). Insets in panels (a) and (d) provide a zoomed view of the dissipation in the vicinity of the particles (green spheres).

Reynolds number is $Re_\lambda = u_{\text{rms}}\lambda/\nu_f$. Here, $u_{\text{rms}} = (2K/3)^{1/2}$ is the root-mean-square velocity. The integral length scale $\mathcal{L} = [3\pi \int_0^\infty \kappa^{-1} \hat{E}(\kappa) d\kappa] [4 \int_0^\infty \hat{E}(\kappa) d\kappa]^{-1}$ is computed from the energy spectrum $\hat{E}(\kappa)$. The latter is defined so that the integral $\int_0^\infty \hat{E}(\kappa) d\kappa$ returns the total kinetic energy of the carrier flow. The eddy turnover time is based on the root-mean-square velocity $\tau_\mathcal{L} = \mathcal{L} [(2/3) \int_0^\infty \hat{E}(\kappa) d\kappa]^{-1/2}$. The definitions of \mathcal{L} and λ stem from the homogeneous and isotropic nature of the carrier flow (Pope 2000, §6.5).

As reported in table 1, the average kinetic energy $\langle K \rangle$, the average dissipation $\langle \varepsilon \rangle$ and the Taylor-Reynolds number Re_λ decrease markedly as M_p increases: a significant

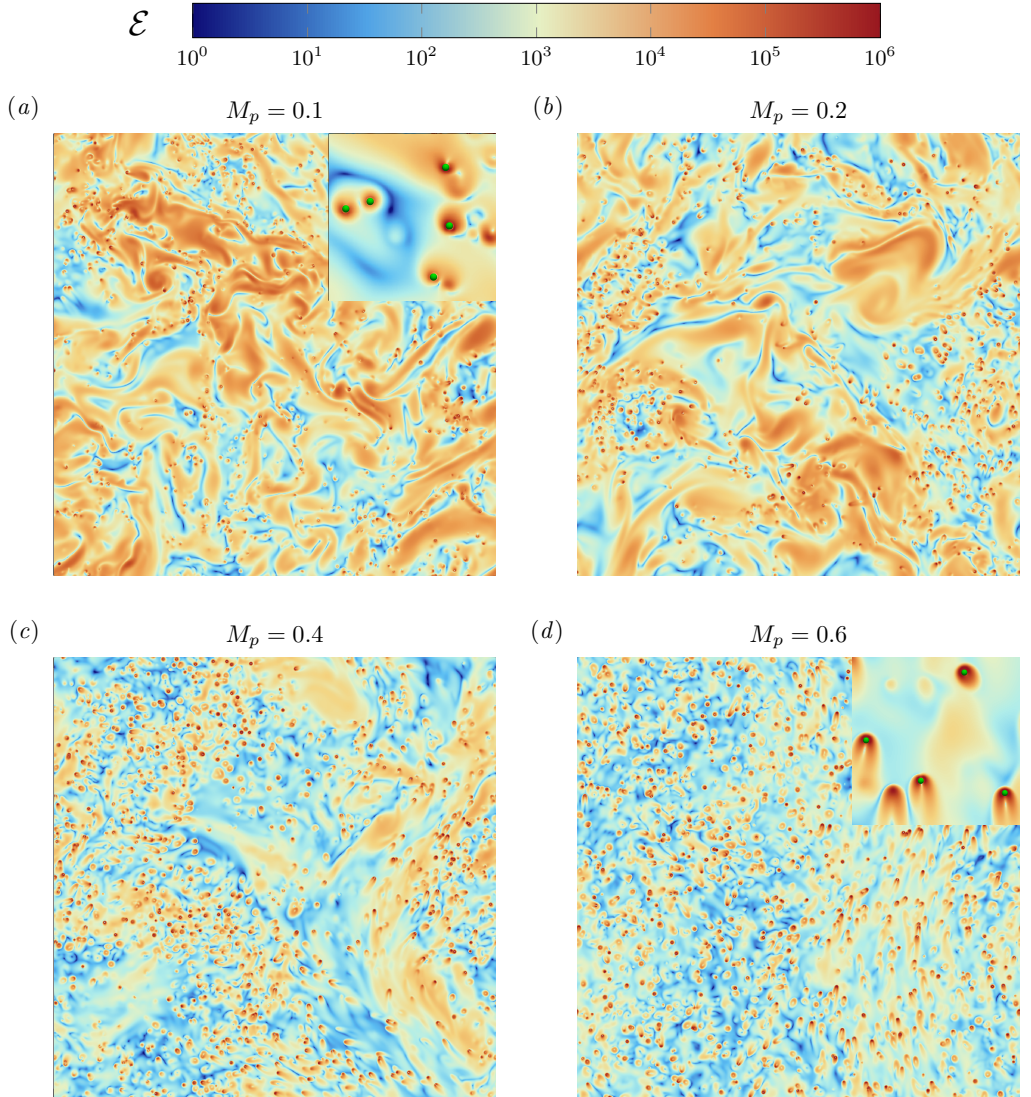


Figure 2. Effect of increasing particle-to-fluid density ratio and mass fraction on the enstrophy, \mathcal{E} . Each panel shows the enstrophy with a logarithmic color scale in a particle-laden domain with different mass fractions: $M_p = 0.1$ (a), 0.2 (b), 0.4 (c), and 0.6 (d). Insets in panels (a) and (d) provide a zoomed view of the enstrophy in the vicinity of the particles (green spheres).

portion of the turbulent kinetic energy is transferred directly to the particles via the fluid-particle forcing f_i^{part} in (2.1a) and the surface integrals in (2.4). The average integral length scale $\langle \mathcal{L} \rangle$ and the average integral time scale $\langle \tau_{\mathcal{L}} \rangle$ of the flow increase slightly with particle inertia, suggesting that the energy density shifts to lower wavenumbers while the intermediate and small-scale structures weaken as M_p increases. The increase of $\langle \mathcal{L} \rangle$ should not be interpreted as the evidence of larger turbulent eddies, but as the disappearance of the intermediate and small ones. Overall, the amount of kinetic energy lost by the carrier flow increases when suspensions of larger mass fraction are considered. In the laden cases, $\langle K \rangle$ decreases as M_p increases from 0.1 to 0.4, while $\langle \varepsilon \rangle$ increases slightly from $M_p = 0.2$ to $X0-8$

Ψ_p	M_p	$\frac{\langle K \rangle}{F_0 L}$	$\frac{\langle \varepsilon \rangle}{(F_0^3 L)^{1/2}}$	$\frac{\langle \eta \rangle}{L}$	$\langle \tau_\eta \rangle \left(\frac{F_0}{L} \right)^{1/2}$	$\frac{\langle \lambda \rangle}{L}$	$\langle Re_\lambda \rangle$	$\frac{\langle \mathcal{L} \rangle}{L}$	$\langle \tau_{\mathcal{L}} \rangle \left(\frac{F_0}{L} \right)^{1/2}$
-	0	2.11	2.40	0.003	0.016	0.07	149.34	0.27	0.25
100	0.1	1.60	1.89	0.003	0.018	0.07	127.29	0.27	0.28
250	0.2	1.47	1.83	0.003	0.018	0.07	117.94	0.29	0.33
666	0.4	1.42	2.03	0.003	0.017	0.06	108.57	0.33	0.37
1499	0.6	1.42	2.07	0.003	0.017	0.06	107.58	0.37	0.40

Table 1. Statistics of the carrier flow. The first row describes the unladen case and the others the laden cases. The temporal averages are denoted by the operator $\langle \cdot \rangle$ and the mass fraction of the solid phase M_p is defined in (2.5). All the quantities are non-dimensional. The bulk kinetic energy $\langle K \rangle$, the bulk dissipation rate $\langle \varepsilon \rangle$, the integral scale \mathcal{L} , the eddy turnover time $\tau_{\mathcal{L}}$, the longitudinal Taylor length scale λ_T and the Taylor-based Reynolds number Re_λ are listed.

Ψ_p	M_p	St_η	$St_{\mathcal{L}}$	Re_p	$\frac{\tilde{U}}{(F_0 L)^{1/2}}$
100	0.1	5	0.36	2.18 ± 1.23	1.45 ± 0.11
250	0.2	12	0.73	2.81 ± 1.49	1.28 ± 0.12
666	0.4	32	1.73	3.83 ± 1.81	1.12 ± 0.10
1499	0.6	71.5	3.56	4.28 ± 1.97	1.13 ± 0.09

Table 2. Particle parameters and statistics for each case considered in the PR-DNSs. Here, the volume fraction $\Phi_p = 10^{-3}$ is constant, $\Psi_p = \rho_p / \rho_f$ is the solid-to-fluid density ratio, M_p is the mass fraction defined in (2.5), $St_\eta = \tau_p / \tau_\eta$ the Stokes number based on the Kolmogorov time, $St_{\mathcal{L}} = \tau_p / \tau_{\mathcal{L}}$ the Stokes number based on the eddy turnover time, Re_p the particle Reynolds number defined in (3.1) and $\tilde{U} (F_0 L)^{-1/2}$ is the non-dimensional particle velocity (see §3.5). The mean and standard deviation of Re_p and $\tilde{U} / (F_0 L)^{1/2}$ are obtained by averaging over the particles.

to $M_p = 0.4$. The Kolmogorov spatial scale η and the temporal scale τ_η are not affected by M_p in any of the cases listed in table 1, thus confirming that $D \cong \eta$. These findings are in good agreement with the laboratory measurements of Tanaka & Eaton (2010), who reported an attenuation of 25% of the average turbulent kinetic energy when seeding a single-phase homogeneous and isotropic turbulent flow at $Re_\lambda \cong 130$ with Kolmogorov-size particles with $D/\eta \cong 2$, $M_p = 0.4$ and $\Phi_p = 1.8 \times 10^{-4}$ (see figure 16 therein). In the present DNSs we observe a 32% decrease of $\langle K \rangle$ when the unladen turbulent flow at $Re_p \cong 150$ is seeded with a suspension of volume fraction $\Phi_p = 10^{-3}$ and mass fraction $M_p = 0.4$.

The properties of the particle phase are summarized in table 2. The particle response time $\tau_p = \Psi_p D^2 / (18 \nu_f)$ (Balachandar & Eaton 2010) and the Stokes number based on the Kolmogorov time scale $St_\eta = \tau_p / \tau_\eta$ increase monotonically with Ψ_p and M_p . For the present simulations, we chose values of Ψ_p and St_η in the same range of those considered in the PR-DNSs of Schneiders *et al.* (2017) and the point-particle DNSs of Mortimer & Fairweather (2020) and Gualtieri *et al.* (2023). The flow in the vicinity of the particles is characterised by the particle Reynolds number

$$Re_p = \frac{\langle |\tilde{U}_i - u_i| \rangle_{sh} D}{\nu_f}, \quad (3.1)$$

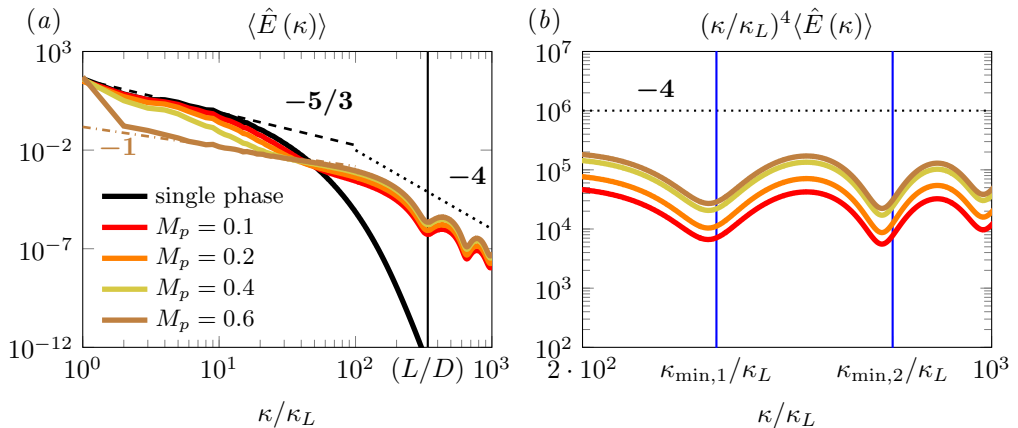


Figure 3. (a) Kinetic energy spectra $\hat{E}(\kappa)$ and (b) compensated energy spectra $(\kappa/\kappa_L)^4 \langle \hat{E}(\kappa) \rangle$, for different mass fraction M_p of the suspension. All wavenumbers are scaled by $\kappa_L = 2\pi/L$. The black dashed line, the brown dash-dot line, and the black dotted line represent the $(\kappa/\kappa_L)^{-5/3}$, $(\kappa/\kappa_L)^{-1}$, and $(\kappa/\kappa_L)^{-4}$ scaling, respectively. The black solid vertical line in (a) denotes the wavenumber of the particle diameter $\kappa/\kappa_L = L/D$, while the blue vertical lines in (b) represent the minima of the high-wavenumber oscillations $\kappa_{min,m} = m\pi/D$, $m \in \mathbb{N}$.

where the difference between the fluid and the particle velocity $\langle |\tilde{U}_i - u_i| \rangle_{sh}$ is estimated by averaging within a spherical shell centred on the particle and with an inner radius $D/2$ and an outer radius $3D/2$ (Uhlmann & Chouippe 2017). As shown in table 2, the particle Reynolds number Re_p increases with the mass fraction, its magnitude for the case $M_p = 0.6$ being almost twice as much as that for the case $M_p = 0.1$. Because D and ν_f are constant in our simulations, the particle Reynolds number (3.1) depends only on the velocity difference $\langle |\tilde{U}_i - u_i| \rangle_{sh}$ and increases as the Stokes number increases. The monotonic increase of Re_p with M_p explains the presence of elongated symmetric wakes observed for some of the particles shown in the visualizations 1 and 2. The dependence of Re_p on St_η is consistent with the numerical results reported by Schneiders *et al.* (2017) and Oka & Goto (2022).

3.2. Kinetic energy spectra and structure functions

To understand how the particles affect the distribution of turbulent kinetic energy across the scales of motion, we compare the kinetic energy spectra $\hat{E}(\kappa)$ computed for different mass fractions M_p . The results are shown in figure 3, where all the spatial wavenumbers κ are scaled with respect to the wavenumber of the domain $\kappa_L = 2\pi/L$. Each curve in figure 3a describes the effect of a different mass fraction M_p . While, the spectra of the unladen case (black curve, $\langle Re_\lambda \rangle \approx 150$) and the case $M_p = 0.1$ (red curve, $\langle Re_\lambda \rangle \approx 127$) feature the classical Kolmogorov scaling $(\kappa/\kappa_L)^{-5/3}$ for $\kappa/\kappa_L < 20$, the spectra obtained for larger M_p depart from such scaling gradually as particle inertia increases. When compared to the unladen case, all the spectra show a lower energy density for $\kappa/\kappa_L < 20$ and a higher energy density at wavenumbers in the dissipative range $\kappa/\kappa_L \geq 10^2$, meaning that Kolmogorov-size particles weaken the large-scale structures of the flow and energise small-scale motions at wavenumbers comparable-to or larger-than the particle wavenumber $\kappa_D = 2\pi/D$ (solid vertical line in figure 3a). This behavior was previously reported in decaying isotropic turbulence (Schneiders *et al.* 2017, see figure 7 therein). These trends of $\hat{E}(\kappa)$ confirm the

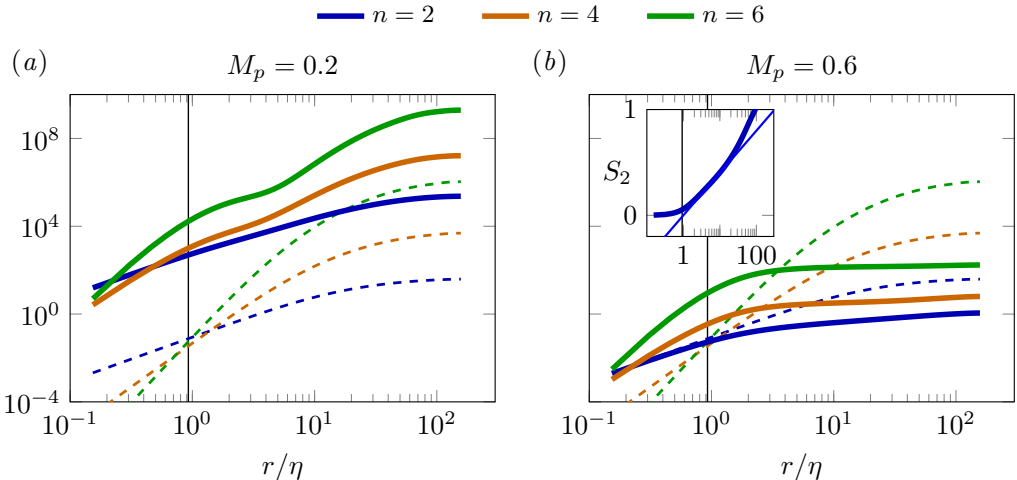


Figure 4. Structure functions of the fluid velocity $\langle S_n \rangle$ with $n = 2, 4, 6$. The thick solid curves represent the laden cases for $M_p = 0.2$ (a) and $M_p = 0.6$ (b), while the structure functions of the unladen flow field are also plotted for comparison with thin, dashed lines. The vertical line denotes the particle diameter normalised with the Kolmogorov length D/η . The inset in (b) compares the semi-logarithmic plot of S_2 (thick blue curve) along with the plot of $\log(r/\eta)$, for $M_p = 0.6$ (thin blue line).

picture shown in figures 1 and 2: high dissipation and high enstrophy concentrate in the particle wakes as the density of the dispersed phase increases.

The amount of kinetic energy transferred to the smallest scales of motion ($\kappa/\kappa_L > 10^2$) increases slightly with M_p . The compensated spectra $(\kappa/\kappa_L)^4 \hat{E}(\kappa)$ shown in figure 3b prove that, in this range, $\hat{E}(\kappa)$ follows the scaling $(\kappa/\kappa_L)^4$ reported by Chiarini *et al.* (2025) for Kolmogorov-size spherical particles of lower density. A similar multiscale behaviour $(\kappa/\kappa_L)^{-3}$ has been reported in the experimental and numerical literature on bubbly flows (e.g. Prakash *et al.* 2016), while laboratory measurements of turbulent flows seeded with Kolmogorov-size particles have not provided a complete characterisation of the energy spectra at high wavenumbers, $O(\eta^{-1})$ (Hwang & Eaton 2006; Poelma *et al.* 2007; Tanaka & Eaton 2010). Recently, Ramirez *et al.* (2024) argued that the sub-particle power-law decay and the periodic oscillations arise from singularities at the interface between the two phases and are artifacts of the Gibbs phenomenon. Their theoretical analysis predicts (i) a power-law decay with exponent $-2q - 2$, where q denotes the order of the singularity, and (ii) oscillations with minima located at $\kappa_{\min,m} = m\pi/D$, with $m \in \mathbb{N}$. High-wavenumber oscillations are clearly visible in figure 3b, and the locations of the minima are in good agreement with $\kappa_{\min,m}$. Although Ramirez *et al.* (2024) focused on droplet-laden flows and did not extend their analysis to solid particles, the absence of a physical cutoff at a maximum wavenumber suggests that the observed $(\kappa/\kappa_L)^{-4}$ scaling may be at least partly influenced by the Gibbs phenomenon.

When the carrier flow is seeded with the heaviest particles (brown curve in figure 3), the kinetic energy spectrum follows the scaling $(\kappa/\kappa_L)^{-1}$ over the range $2 \leq \kappa/\kappa_L < 70$ (brown dash-dot line in figure 3a). The same scaling was reported by Olivier *et al.* (2022a) in flows laden with slender fibres of Kolmogorov-scale cross section. In that study, the authors argued that heavier fibres (M_p) acted as barriers between points separated by distances larger than the fibre cross section, thereby decorrelating the flow and modifying both the exponent of the second-order structure function and the scaling of the energy spectrum $\hat{E}(\kappa)$. To assess whether an analogous mechanism operates in the presence of heavy

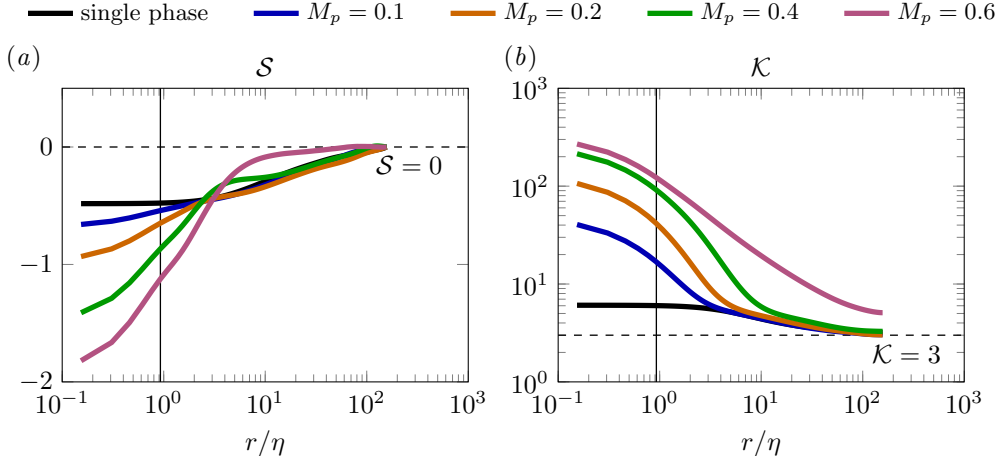


Figure 5. (a) Skewness S and (b) kurtosis \mathcal{K} of the velocity field for increasing particle density ρ_p . The vertical line denotes the particle diameter normalised with the Kolmogorov length D/η . The horizontal dashed line represent the values $S = 0$ in plot (a) and $\mathcal{K} = 3$ in plot (b).

Kolmogorov-size particles, we compute the longitudinal structure functions of the carrier flow $S_n(r) = \langle [\delta u(r, t)]^n \rangle$, where $\delta u(r, t) = [\mathbf{u}(\mathbf{x} + \mathbf{r}, t) - \mathbf{u}(\mathbf{x}, t)] \cdot \mathbf{r}/|\mathbf{r}|$ denotes the longitudinal velocity increment (Pope 2000, §6.7.2). Figure 4 shows the second- ($n = 2$), fourth- ($n = 4$), and sixth-order ($n = 6$) structure functions. The laden cases (thick solid lines) for $M_p = 0.2$ (panel a) and $M_p = 0.6$ (panel b) are compared with the unladen case (thin dashed lines). As particle inertia increases, both the magnitude and the slope of the structure functions decrease markedly. In the heaviest-particle case, the fourth- and sixth-order structure functions approach a plateau and their growth saturates at scales much smaller than the computational domain. Beyond $r > \eta$, the structure functions no longer exhibit power-law behavior. The inset in figure 4b shows a semi-logarithmic plot of the second-order structure function (thick curve), compared with $\log(r/\eta)$ over the interval $1 \leq r/\eta < 10^2$. In homogeneous and isotropic turbulence, the observed asymptotic scaling $S_2 \sim \log(r/\eta)$, valid for $r\kappa \gg 1$, is consistent with the spectral scaling $\hat{E}(\kappa) \sim \kappa^{-1}$. Moreover, the saturation of the structure function signals the loss of velocity autocorrelation (Pope 2000, §6). Taken together, these results indicate that heavy Kolmogorov-scale particles locally decorrelate the turbulent flow field over distances exceeding the particle diameter D .

It is important to note that the weakening of the large-scale structures does not result in an attenuation of the turbulent fluctuations nor in the laminarisation of the flow. On the contrary, the intense velocity gradients in the particles' wakes, shown in the visualizations 1 and 2, indicate enhanced small-scale activity. The deviation of the higher-order moments from the predictions of Kolmogorov theory has been observed in recent PR-DNSs of finite-size and Kolmogorov-size particles (Chiarini & Rostí 2024; Chiarini *et al.* 2025). To quantify the degree of the flow intermittency (i.e. the relevance of localised events that break the similarity hypothesis), we follow the extended-similarity framework of Benzi *et al.* (1993) and examine the ratio of the structure functions $S_n/(S_2)^{n/2}$. A departure from the self-similar scaling $S_n/(S_2)^{n/2} = O(1)$ signals the onset of intermittency. We therefore compute the skewness $S = S_3/S_2^{3/2}$ and the kurtosis $\mathcal{K} = S_4/S_2^2$ to investigate the effect of increasing particle inertia on small-scale intermittency. Results are shown in figure 5a (S) and 5b (\mathcal{K}). At distances $r < D$ (vertical black line in figure 5), the magnitude

of S and \mathcal{K} increase monotonically with increasing mass fraction M_p , meaning that the deviation from similarity is stronger when heavier particles are considered. This result agrees with the behavior of finite-size particles (Chiarini & Rosti 2024) and Kolmogorov-size particles with $\Phi = 10^{-3}$ and $\Psi_p \leq 100$ (Chiarini *et al.* 2025). However, at larger distances, the skewness and kurtosis exhibit opposite behaviour: as M_p increases, the skewness decays more rapidly and approaches the asymptote $S = 0$ (horizontal dashed line), while the kurtosis increases abruptly for $M_p = 0.6$ (magenta curves in figure 5) and departs completely from the Gaussian value $\mathcal{K} = 3$. In the heaviest-particle case, deviations of \mathcal{K} are observed at all separations, suggesting that heavy Kolmogorov-scale particles enhance flow intermittency over scales much larger than the particle diameter D , thereby altering the inertial cascade and breaking the similarity hypothesis.

3.3. Scale-by-scale energy budget

The terms of the kinetic energy balance equation provide additional insights into the modulation of the carrier flow. By expressing them as a function of the spatial wavenumber κ , one can quantify the energy production, transfer and depletion across the scales of motion. The terms are obtained by contracting the Fourier transform of the momentum balance (2.1a) with that of the velocity field \hat{u}_i (Pope 2000; Olivieri *et al.* 2022b). The pressure term vanishes because of (2.1b) and the resulting terms are then integrated from a given non-zero wavenumber to infinity, yielding the kinetic energy balance in the spectral domain

$$\begin{aligned} \frac{\partial}{\partial t} \int_{\kappa}^{\infty} \hat{u}_i \hat{u}_i^* d\tilde{\kappa} + \underbrace{\frac{1}{2} \int_{\kappa}^{\infty} (\hat{G}_i \hat{u}_i^* + \hat{G}_i^* \hat{u}_i) d\tilde{\kappa}}_{-\Pi(\kappa)} + \underbrace{\int_{\kappa}^{\infty} \tilde{\kappa}^2 \nu_f \hat{u}_i \hat{u}_i^* d\tilde{\kappa}}_{\mathcal{D}_v(\kappa)} = \\ = \underbrace{\frac{1}{2} \int_{\kappa}^{\infty} (\hat{f}_i^{ABC} \hat{u}_i^* + \hat{f}_i^{ABC*} \hat{u}_i) d\tilde{\kappa}}_{P(\kappa)} + \underbrace{\frac{1}{2} \int_{\kappa}^{\infty} (\hat{f}_i^{\text{part}} \hat{u}_i^* + \hat{f}_i^{\text{part}*} \hat{u}_i) d\tilde{\kappa}}_{\Pi_p(\kappa)}. \quad (3.2) \end{aligned}$$

Here, $\hat{G}_i = i\kappa_j \widehat{u_j u_i}$ is the Fourier transform of the nonlinear terms, and the superscript $*$ denotes the complex conjugate. The integral $\Pi(\kappa)$ is the flux of the nonlinear terms, $\Pi_{fs}(\kappa)$ the flux of the particle forcing, and the integral P the energy injected in the system by the ABC forcing (2.2). The integral $\mathcal{D}_v(\kappa)$ is conveniently expressed as the sum of the bulk dissipation $\varepsilon = \mathcal{D}_v(0)$ and the viscous dissipation integral $D_v(\kappa)$

$$\mathcal{D}_v(\kappa) = \underbrace{\mathcal{D}_v(0)}_{\varepsilon} - \underbrace{\int_0^{\kappa} \tilde{\kappa}^2 \nu_f \hat{u}_i \hat{u}_i^* d\tilde{\kappa}}_{D_v(\kappa)}. \quad (3.3)$$

Time-averaging (3.2) yields the scale-by-scale energy budget for a steady-state flow

$$\langle \Pi(\kappa) + P(\kappa) + \Pi_p(\kappa) + D_v(\kappa) \rangle = \langle \varepsilon \rangle. \quad (3.4)$$

The ABC forcing (2.2) is a Dirac delta centred at $\kappa = \kappa_L$ and the integral

$$P(\kappa) = \begin{cases} \frac{1}{2} (\hat{f}_i^{ABC} \hat{u}_i^* + \hat{f}_i^{ABC*} \hat{u}_i) & \text{if } \kappa \leq \kappa_L, \\ 0 & \text{if } \kappa > \kappa_L, \end{cases} \quad (3.5)$$

has a single non-zero value at $\kappa/\kappa_L = 1$ in figure 6 (orange dot). Hence, for any $\kappa > \kappa_L$, the temporal average of (3.4) reduces to $\langle \Pi + \Pi_{fs} + D_v \rangle / \langle \varepsilon \rangle = 1$.

Each of the four panels in figure 6 shows the terms of (3.4) as functions of κ/κ_L , for a given M_p , with all terms normalized by $\langle \varepsilon \rangle$. Note that, the curves of $\langle \Pi \rangle$ and $\langle D_v \rangle$

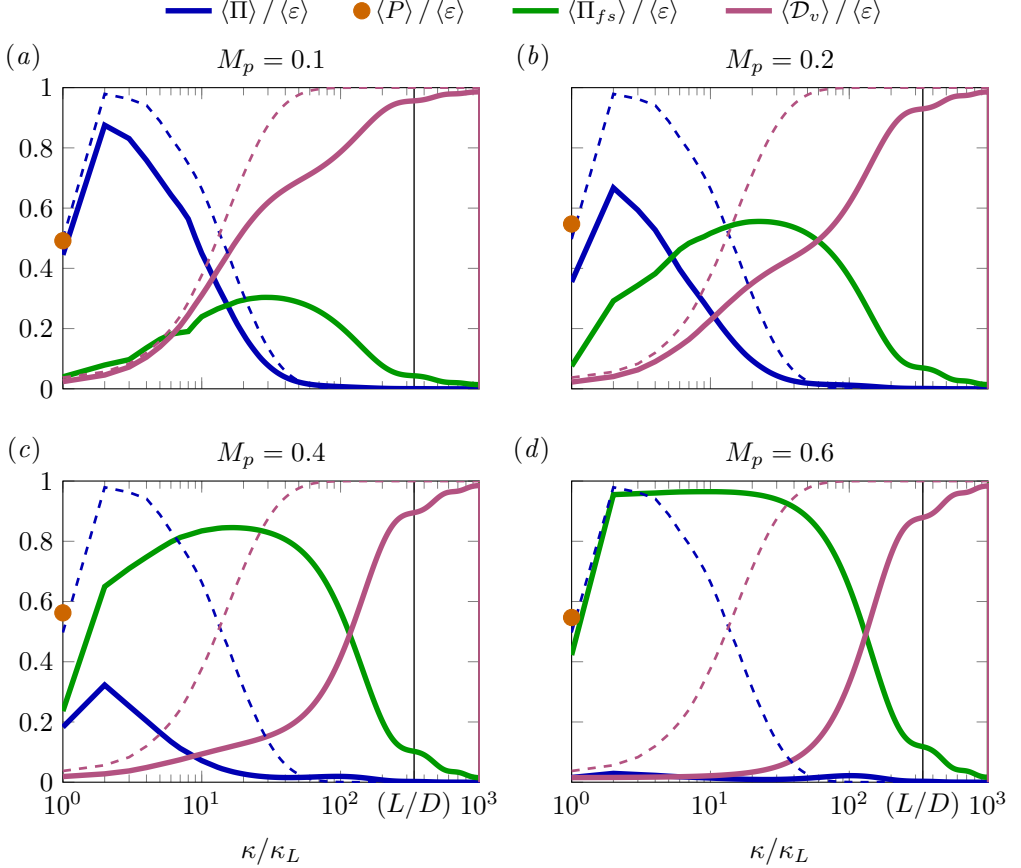


Figure 6. Scale-by-scale energy budget (3.4) for increasing particle inertia. The thick, solid curves represent the turbulent transport term (blue), particle forcing term (green) and dissipation term (magenta) of the cases $M_p = 0.1$ (a), $M_p = 0.2$ (b), $M_p = 0.4$ (c) and $M_p = 0.6$ (d). The ABC forcing f_i^{ABC} fuels the large-scale motions at $\kappa = \kappa_L$ (orange dot) via the integral (3.5). The turbulent transport (blue) and dissipation (magenta) of the unladen case are plotted with the thin dashed curves for comparison. The black, solid vertical line denotes the wavenumber of the particle diameter $\kappa_D / \kappa_L = L/D$.

are also reported for the unladen case with thin, dashed lines. In the light-particle case ($M_p = 0.1$), the magnitude of the nonlinear flux $\langle \Pi \rangle$ (dark blue) is essentially the same as in the unladen case, and the effect of the particle forcing $\langle \Pi_{fs} \rangle$ (green) is rather limited. Indeed, the energy transfer is dominated by the nonlinear transfer $\langle \Pi \rangle$ and the dissipation $\langle D_v \rangle$ at all scales. This result suggests that the inertial cascade is still active in the range $\kappa / \kappa_L < 20$, consistently with the $-5/3$ scaling of the spectra in figure 3 (red curve therein). Figures 6b,c show that the energy flux of the turbulent cascade $\langle \Pi \rangle$ (dark blue) decreases, while the fluid-particle interaction term $\langle \Pi_{fs} \rangle$ (green) increases, gradually as particle inertia increases. In the heaviest case ($M_p = 0.6$), the contribution of the dissipation and nonlinear terms become negligible at large and intermediate scales, where the energy transfer is dominated by the fluid-particle interaction. The contribution of the nonlinear terms is virtually zero at the particle scale ($\kappa / \kappa_L = L/D$, black vertical line) for all the laden cases. There, $\langle \Pi_{fs} \rangle$ is much smaller than $\langle D_v \rangle$ but increases sensibly with M_p . The increase of both $\langle \Pi_{fs} \rangle$ and $\langle D_v \rangle = \varepsilon - \langle \Pi \rangle$ at $\kappa \cong \kappa_D$ for increasing M_p was also

reported by Schneiders *et al.* (2017, see figure 7 therein). These findings are consistent with the relatively small values of the particle Reynolds number Re_p (see table 2) and the short, symmetric laminar wakes shown in the insets in figure 1*d* and 2*d*.

The kinetic energy spectra shown in figure 3 and the scale-by-scale energy budget shown in figure 6 support the argument that small, yet heavy particles influence energy transfer at scales much larger than their size. While the presence of Kolmogorov-size particles with moderate M_p mainly influences the local topology of the flow at the smallest scales, high-density suspensions significantly alter the large-scale structures of the flow. In this limit, the kinetic energy balance is dominated by the fluid-particle interaction and the nonlinear fluxes become negligible, significantly departing from the typical Kolmogorov turbulence.

3.4. Velocity gradient tensor and small-scale intermittency

The visualizations in figures 1 and 2 depict a pronounced shift in the local distribution of the dissipation rate ε and the enstrophy \mathcal{E} as particle inertia increases. The peak values of ε and \mathcal{E} are no longer distributed across large turbulent structures but instead become confined to the vicinity of the particles. In this section, we examine the properties of the velocity gradient tensor to gain further insight into the resulting local flow structures.

The velocity gradient tensor $\partial_j u_i$ can be decomposed into its symmetric part, $S_{ij} = (\partial_j u_i + \partial_i u_j)/2$, and its skew-symmetric part, $W_{ij} = (\partial_j u_i - \partial_i u_j)/2 = -\epsilon_{ijk} \omega_k/2$. The latter is related to the local vorticity $\omega_i = -\epsilon_{ijk} \partial_j u_k = -\epsilon_{ijk} \dot{W}_{jk}$ (Meneveau 2011; Davidson 2015). The symmetric part S_{ij} is a diagonal tensor in the frame of reference of its principal axes, the diagonal elements being the three principal rates of strain $|\alpha| \geq |\beta| \geq |\gamma|$, with $\alpha + \beta + \gamma = 0$ for the incompressibility constraint (2.1*b*). The eigenvalues of $\partial_j u_i$ satisfy the depressed cubic equation

$$\lambda^3 + Q\lambda + R = 0, \quad (3.6)$$

where Q and R are the second and the third invariants of $\partial_j u_i$

$$Q = -\frac{1}{2} (\alpha^2 + \beta^2 + \gamma^2) + \frac{1}{4} (\omega_x^2 + \omega_y^2 + \omega_z^2), \quad (3.7a)$$

$$R = -\alpha\beta\gamma - \frac{1}{4} (\alpha\omega_x^2 + \beta\omega_y^2 + \gamma\omega_z^2), \quad (3.7b)$$

respectively. The sign of Q determines whether the local small-scale fluid motion is characterised by strong vorticity ($Q \gg 1$) or large axial strain ($-Q \gg 1$). In the former case, $Q \sim (\omega_x^2 + \omega_y^2 + \omega_z^2)/4$, $R \sim -(\alpha\omega_x^2 + \beta\omega_y^2 + \gamma\omega_z^2)/4$ and the discriminant of (3.6) $\Delta = -4Q^3 - 27R^2 < 0$, meaning that the velocity gradient tensor has one real and two complex conjugate eigenvalues. Positive and negative values of R describe vortex stretching and vortex compression, respectively (Cantwell 1992). Conversely, when Q is large and negative, the small scales are dominated by axial strain and $R \sim -\alpha\beta\gamma$. Positive and negative values of R describe biaxial strain ($\alpha > 0$) and axial strain ($\alpha < 0$), respectively. In homogeneous and isotropic turbulence, the average of the invariants Q and R is zero and the global generation of enstrophy can be expressed purely in terms of the axial strain $-\langle \alpha\beta\gamma \rangle$ (Betchov 1956).

Small-scale intermittency drives large negative excursions of Q and positive excursions of R (biaxial strain), leading to sling events that enhance small-particle collisions (Codispoti *et al.* 2025). This behaviour is observed in the probability density functions (PDFs) in figure 7, where the distributions of the laden cases (coloured curves) are compared to those obtained from an unladen homogeneous and isotropic turbulent flow field. The values of Q and R are scaled with the Kolmogorov time τ_η . Increasing particle inertia intensifies large negative excursions of Q (see figure 7*a*) and enhances strain at the expense of enstrophy.

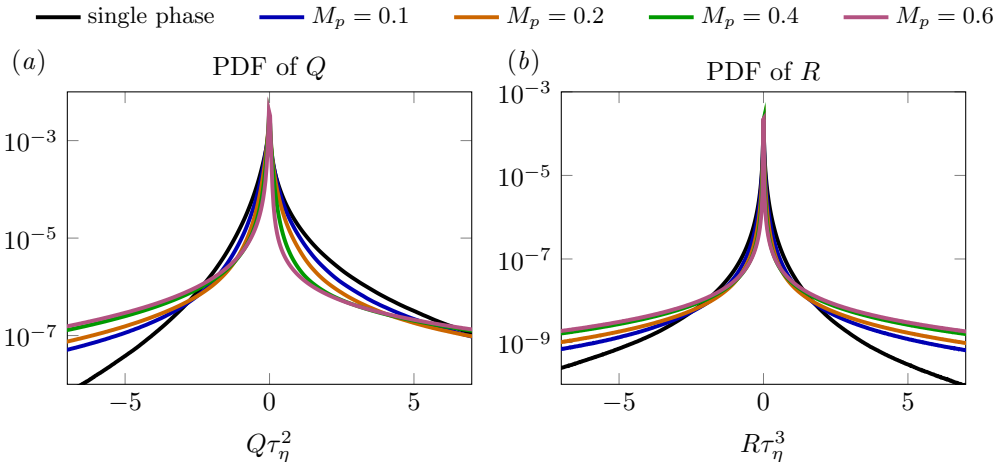


Figure 7. Probability density function (PDF) of (a) the second invariant Q (3.7a) and (b) the third invariant R (3.7b) of the velocity gradient tensor $\partial_j u_i$ for increasing mass fraction M_p (solid coloured curves) and in the unladen case (solid black curves). The values of Q and R are normalised with the Kolmogorov time τ_η .

Note that the positive and negative tails of these distributions also grow when the flow is laden with lighter particles, as previously reported by Chiarini *et al.* (2025) for $\Psi_p = 100$ and $\Phi_p = 10^{-3}$. These effects become more and more marked as Ψ_p and M_p increase, and the PDF of Q becomes more negatively skewed as M_p increases (coloured curves 7a). Conversely, the distribution of R becomes progressively symmetric as M_p increases (see figure 7b), thus indicating an equilibrium between axial and biaxial strain and vortex stretching or compression.

More insights can be obtained from the joint probability density functions (JPDF), shown in figure 8. The black curves show the contours of constant probability density with uniform logarithmic spacing in the range 10^{-3} (outermost curve) to 10^1 (innermost curve). The fluid phenomena prescribed by the sign of the invariants are summarised in the four quadrants of figure 8a. In the unladen case (figure 8a), vortex stretching is predominant in high-ensrophy regions ($Q > 0, R < 0$), while strain-dominated regions ($Q < 0, R > 0$) are characterised by biaxial strain, as shown by the high-probable events located along the positive- R branch of the Vieillefosse tail, i.e. the zero-discriminant curve $Q = -3(R/2)^{2/3}$ (blue curve in figure 8). The shape of the JPDF changes considerably as the density of the suspension increases (figures 8b and 8c). The distributions become more and more symmetric with respect to the vertical axis $\langle R \rangle = 0$, with high-ensrophy events becoming progressively less common, although vortex stretching remains slightly predominant in the $Q > 0$ region. Strain events become more common as the JPDF spread along the negative- R branch of the Vieillefosse tail (figures 8c and 8d), meaning that axial and biaxial strain are equally likely to occur when the flow is laden with heavy particles.

These results agree with the analysis of Chiarini *et al.* (2025), but show some discrepancy with those of Schneiders *et al.* (2017), who investigated a decaying homogeneous and isotropic flow laden with very heavy suspensions (up to $\Psi_p = 5000$) at much lower Reynolds numbers ($Re_\lambda \leq 50$). In contrast to the present findings, they did not observe the onset of strain-dominated events along the negative- R branch of the Vieillefosse tail, which is associated with an intensification of axial strain and turbulent dissipation.

— JPDF — $\Delta = 0$

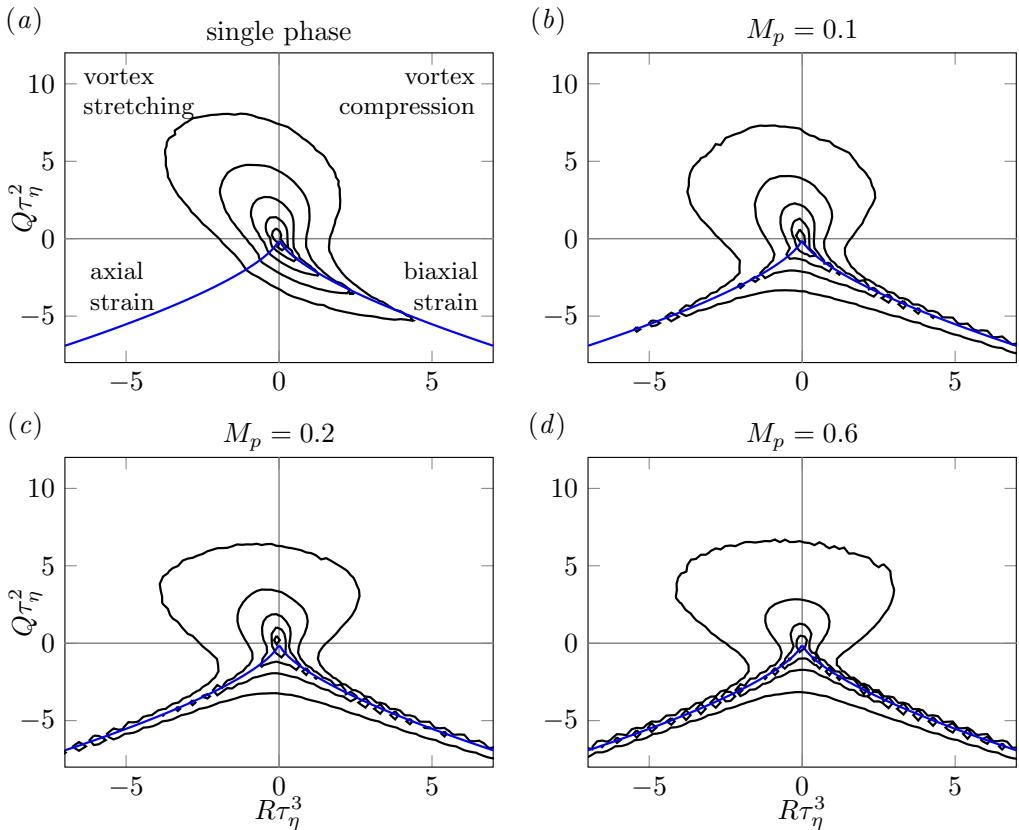


Figure 8. Joint probability density function (JPDF) of the invariants Q and R of the velocity gradient tensor $\partial_j u_i$ for increasing solid mass fraction M_p . The invariants are normalized on the Kolmogorov time scale τ_η . The five black curves in each panel represent isolines of constant JPDF with uniform logarithmic spacing (from the outermost 10^{-3} to the innermost 10^1). The blue curves describe the two branches of the Vieillefosse tail $Q = -3(R/2)^{2/3}$, i.e. the points where the discriminant of equation (3.6) is zero.

3.5. Particle velocities and trajectories

We briefly investigate the effect of particle inertia on particle motion. Figure 9a shows the probability density function (PDF) of the magnitude of the particle velocity, $|\tilde{U}_i|$, computed over the entire time history of each particle for increasing values of the mass fraction M_p . For all laden cases (coloured curves), the PDFs closely match Gaussian distributions with the same mean $\mu_{\tilde{U}_i}$ and standard deviation $\sigma_{\tilde{U}_i}$ (dashed curves), whose values are reported in the rightmost column of table 2. The normality of the distributions is further confirmed by rescaling the PDFs using the variable $Z_{\tilde{U}_i} = (|\tilde{U}_i| - \mu_{\tilde{U}_i})/\sigma_{\tilde{U}_i}$: the results in the inset of figure 9a show an excellent collapse. The mean particle velocity decreases as M_p increases from 0.1 to 0.4 but remains approximately constant for M_p between 0.4 and 0.6, as indicated by the overlap of the green and magenta curves. Heavier particles are therefore slower in the reference frame of the computational domain but, since their particle Reynolds number Re_p increases (see table 2), they are also slightly faster relative to the surrounding fluid.

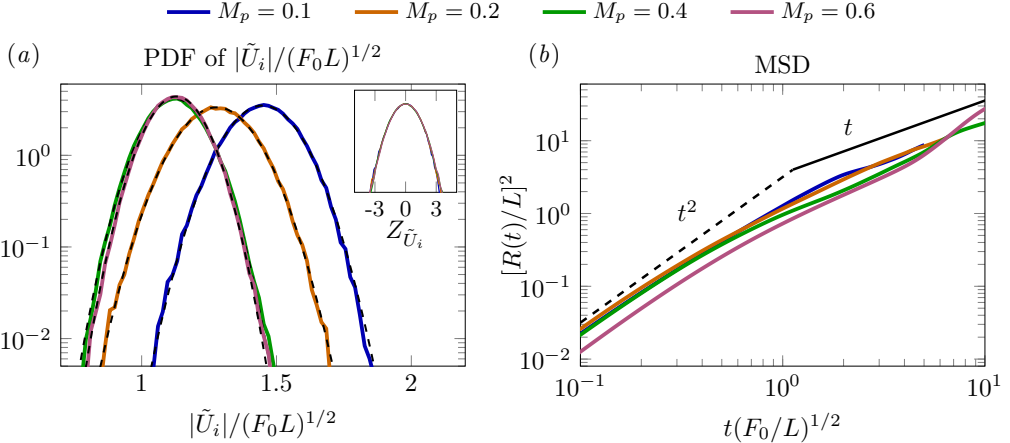


Figure 9. (a) PDF of the absolute value of the particle velocity $|\tilde{U}_i|$ for increasing particle inertia (thick, coloured curves). The distributions overlap with the Gaussian curves (thin, dashed, black curves). The PDFs are rescaled with respect to the reference velocity $(F_0 L)^{1/2}$. The inset shows the PDFs of the normalised variable $Z_{\tilde{U}_i} = (|\tilde{U}_i| - \mu_{\tilde{U}_i})/\sigma_{\tilde{U}_i}$. (b) Mean square displacement $[R(t)]^2$ of the particles for increasing particle inertia (coloured curves). The time is scaled by a factor $(L/F_0)^{1/2}$ and the displacement by L . The results are compared with the scalings $[R(t)]^2 \sim t^2$ (black dashed line) and $[R(t)]^2 \sim t$ (black solid line).

We further characterise particle motion by computing the temporal evolution of the mean square displacement,

$$[R(t)]^2 = \langle |X_i(t) - X_i(0)|^2 \rangle_p, \quad (3.8)$$

where X_i denotes the particle position and $\langle \cdot \rangle_p$ indicates averaging over the N particles. The results, shown in figure 9b, reveal a ballistic regime $[R(t)]^2 \sim t^2$ at short times $t \ll 1$, independent of M_p (dashed black line), in agreement with previous observations for finite-size spherical particles (Chiarini *et al.* 2024). Here, the time is scaled by a factor $(L/F_0)^{1/2}$ and the displacement by L . For times $t = O(1)$, the mean square displacement departs from the ballistic regime. At later times, the cases with $M_p = 0.2$ and $M_p = 0.4$ approach the Brownian asymptote $\sim t$, although they do not collapse perfectly onto it (solid line). In contrast, the heaviest case ($M_p = 0.6$, magenta curve) does not reach a clear asymptotic scaling, probably because the temporal history of the particle trajectories available in the present simulations is not long enough. Overall, we observe a progressive longer time to depart from the ballistic regime, as the inertia of the particle increases.

3.6. Particle clustering

We examine the effect of particle inertia on cluster formation in this section. Particle clustering is quantified using a Voronoi tessellation, in which the computational domain is partitioned into N polyhedra – one associated with each particle – referred to as Voronoi volumes. The Voronoi volume of a particle consists of all points in space that are closer to that particle than to any other. As a result, smaller Voronoi volumes are found in regions of high particle concentration, whereas larger volumes indicate dilute regions. The Voronoi volume associated with a given particle evolves in time according to its position X_i relative to its neighbours (Monchaux *et al.* 2010), and therefore provides a reliable local measure of the particle concentration (Fiabane *et al.* 2012). Owing to its locality in both space and time, the Voronoi tessellation captures the spatial structure of particle clusters, as well as their temporal evolution (Uhlmann & Chouippe 2017). In the present study, we computed

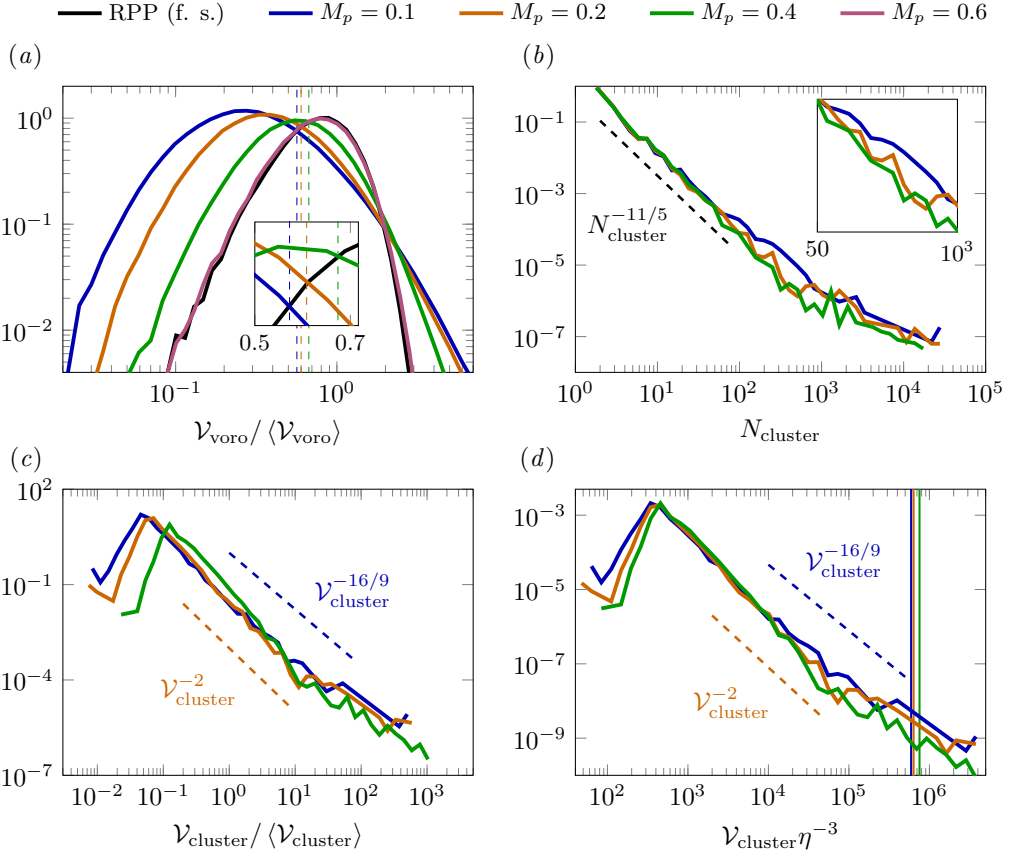


Figure 10. (a) PDFs of the normalised Voronoi volumes $\mathcal{V}_{\text{voronoi}} / \langle \mathcal{V}_{\text{voronoi}} \rangle$ for increasing particle-to-fluid density ratio Ψ_p and mass fraction M_p (blue, orange and green) are compared to that obtained for a suspension of finite-size (f. s.) particles distributed via a random-Poisson process (RPP, black). The inset shows the position of the lower cross-over points (LCO) listed in table 3 (dashed vertical lines). (b) PDF of the number of particles forming a cluster N_{cluster} . The inset shows a zoomed view of the PDFs in the range $50 < N_{\text{cluster}} < 10^3$. (c) PDF of the cluster volumes normalised on the average $\langle \mathcal{V}_{\text{cluster}} \rangle$ (solid lines), along with the scaling -2 and $-16/9$ (dashed lines). (d) PDF of the cluster volumes normalised on η^3 (solid lines), along with the scaling -2 and $-16/9$ (dashed lines). The solid vertical line denote a normalised cluster volume equal to the cube of the integral scale $\mathcal{L}^3 \eta^{-3}$.

the three-dimensional Voronoi tessellation using an in-house code based on the C++ library [Voro++](#) (Lu *et al.* 2023).

The tendency of particles to form clusters is examined by comparing the probability density functions (PDFs) of the Voronoi volumes obtained from the PR-DNSs with those computed for a population of finite-size particles whose spatial coordinates are assigned through a random Poisson process (RPP). The time-averaged PDFs of the Voronoi volumes $\mathcal{V}_{\text{voronoi}}$ obtained from the DNSs are plotted for increasing mass fraction M_p (coloured curves) in figure 10a. The PDF of a population of N non-overlapping, Kolmogorov-size particles distributed through a RPP is plotted in black for comparison. All the PDFs in figure 10a were rescaled on the inverse of the global concentration $\langle \mathcal{V}_{\text{voronoi}} \rangle = L^3 / N = 1.35 \times 10^{-5}$ (Fiabane *et al.* 2012). The departure of the PDFs from the RPP case is maximum in the light-particle case $M_p = 0.1$ (blue curve), while the PDFs approach the RPP case gradually as Ψ_p and M_p increase, ultimately collapsing on the RPP case for $M_p = 0.6$. These PDFs

Ψ_p	M_p	σ_{voro}	S_{voro}	$\mathcal{K}_{\text{voro}}$	LCO	HCO	$(\langle \mathcal{V}_{\text{cluster}} \rangle)^{1/3} \eta^{-1}$	$\langle N_{\text{cluster}} \rangle$
100	0.1	1.37	5.58	56.20	0.57	1.96	19.62	54
250	0.20	1.24	6.18	71.15	0.60	1.95	18.60	41
666	0.40	0.74	3.19	24.87	0.67	1.82	15.42	19
1499	0.60	0.44	0.93	4.37	n.a.	n.a.	n.a.	n.a.
RPP (finite size)		0.42	0.80	3.90	n.a.	n.a.	n.a.	n.a.

Table 3. Properties of the Voronoi tessellation. The table lists the standard deviation σ , skewness S , and kurtosis \mathcal{K} of the normalised Voronoi volumes $\mathcal{V}_{\text{voro}}/\langle \mathcal{V}_{\text{voro}} \rangle$, along with the lower cross-over points (LCO) and the higher cross-over points (HCO) of their PDFs. The two rightmost columns list the characteristic cluster length $(\langle \mathcal{V}_{\text{cluster}} \rangle)^{1/3}/\eta$ and the average number of particles forming a cluster $\langle N_{\text{cluster}} \rangle$. All variables are non-dimensional.

have unit mean and their broadening indicates the presence of Voronoi volumes that are either smaller (concentrated regions) and larger (dilute regions) than those computed for the RPP. Monchaux *et al.* (2010) showed that the PDFs of Voronoi areas of two-dimensional tessellations are well-approximated by log-normal distributions, whereas Tagawa *et al.* (2012) pointed out that a Gamma distribution better interpolates the PDFs of Voronoi volumes in three-dimensional tessellations. Either way, the log-normal and the Gamma distributions that fit the PDFs of $\mathcal{V}_{\text{voro}}/\langle \mathcal{V}_{\text{voro}} \rangle$ are characterised by the standard deviation σ_{voro} , which quantifies the degree of clustering (Monchaux *et al.* 2010).

The statistical properties of the Voronoi tessellation are listed in table 3. The standard deviation σ_{voro} is maximum for $M_p = 0.1$ ($St_\eta = 5$) and decreases monotonically as the PDFs of the Voronoi volumes approach the RPP case (black curve in figure 10a) for large M_p . The probability of large-concentration events is therefore maximum for $M_p = 0.1$ and decreases for larger M_p . While the PDFs for $M_p = 0.2$ and $M_p = 0.4$ reveal a moderate presence of clustering events, the distribution for the heaviest-particle case $M_p = 0.6$ ($St_\eta = 71.5$, magenta curve) collapses on that of the RPP, meaning that clustering does not occur in this case. Similarly, the skewness S_{voro} and the kurtosis $\mathcal{K}_{\text{voro}}$ are maximum for $M_p = 0.2$ and approach the RPP values for $M_p = 0.6$. Although the degree of clustering (i.e. σ_{voro}) decreases for decreasing Re_λ and increasing St_η , separating the effect of each parameter is not straightforward (Hassaini *et al.* 2023). Sumbekova *et al.* (2017) measured the clustering of polydisperse smaller-than-Kolmogorov particles in homogeneous and isotropic turbulence and reported a weak influence of St_η and a strong influence of Re_λ and Φ_p on σ_{voro} . However, the DNS data reviewed by Monchaux (2012) reveal a marked influence of the Stokes number on the degree of clustering. In the present work, increasing M_p from 0.4 and 0.6 results in the reduction of σ_{voro} from 0.74 to 0.44 and in the increase of St_η from 32 to 71.5, but does not affect Re_λ sensibly (see tables 3, 2 and 1). For an unladen Taylor-Reynolds number $Re_\lambda \approx 140$ and same volume fraction $\Phi_p = 10^{-3}$, Chiarini *et al.* (2025) reported clustering intensification when the density ratio Ψ_p increased from 5 to 100. The present results show that the opposite occurs when Ψ_p increases from 100 to values typical of gas-solid mixtures $O(10^3)$ (Rose & Durant 2009).

We follow the criterion proposed by Monchaux *et al.* (2010) to study the spatial extension of the particle clusters. The PDFs obtained from the PR-DNSs intersect that of the RPP case for two values of $\mathcal{V}_{\text{voro}}/\langle \mathcal{V}_{\text{voro}} \rangle$. Voronoi cells smaller than the low cross-over points (LCO) are flagged as dense and may be part of a cluster. Conversely, cells greater than the high cross-over point (HCO) belong in void regions. The LCO points and the HCO points are listed in table 3 and are denoted by the dashed vertical lines in figure 10a (see also the inset for an enlarged view). Although two cross-over points exist in the case $M_p = 0.6$, the

clustering criterion of Monchaux *et al.* (2010) can not be applied because the curves of the RPP case and the heaviest case ($M_p = 0.6$) almost overlap and their normalised standard deviation is approximately the same (see table 3). Thus, we discuss clustering for the cases $M_p = 0.1, 0.2$ and 0.4 .

The condition $\mathcal{V}_{\text{voro}}/\langle \mathcal{V}_{\text{voro}} \rangle < \text{LCO}$ is necessary but not sufficient for a particle to be considered part of a cluster (Baker *et al.* 2017). Accordingly, only dense Voronoi cells that share at least one vertex are regarded as part of the same cluster (Hassaini *et al.* 2023). For each dense cell, its neighbours are examined to identify adjacent dense cells, which are then grouped into a single cluster. A minimum of two contiguous dense cells is required to define a cluster, and a cell cannot belong to multiple clusters. To prevent the unphysical merging of adjacent yet distinct clusters, dense-cell particles separated by a distance larger than the cut-off ($\langle \mathcal{V}_{\text{voro}} \rangle^{1/3}$) are excluded.

The PDFs of the number of particles forming a cluster N_{cluster} are shown in figure 10b. The distributions are in qualitative agreement with those of Uhlmann & Chouippe (2017) (refer to figure 10a therein) who performed PR-DNS of spherical particles with $D/\eta = 5$ in homogeneous and isotropic turbulence. These PDFs collapse for $N_{\text{cluster}} < 10^2$ where they show a power-law dependency $N_{\text{cluster}}^{-11/5}$ which is not influenced by particle inertia. They depart for larger N_{cluster} , meaning that large clusters are less likely to form as M_p increases (see inset in figure 10b). The average number of particles per cluster, listed in table 3, diminishes markedly as M_p increases.

The PDFs of the cluster volumes $\mathcal{V}_{\text{cluster}}$ are shown in figure 10c and 10d, where they are rescaled on the average $\langle \mathcal{V}_{\text{cluster}} \rangle$ (Sumbekova *et al.* 2017) and the cube of the Kolmogorov scale η (Uhlmann & Chouippe 2017; Hassaini *et al.* 2023). These PDFs exhibit a distinct peak followed by a power-law decay which suggests the existence of a characteristic cluster size. The characteristic length $\langle \mathcal{V}_{\text{cluster}} \rangle^{1/3}$ (Rostami *et al.* 2024) ranges between 10η and 20η (see table 3), in close agreement with laboratory measurements of polydisperse distributions (Obligado *et al.* 2014; Sumbekova *et al.* 2017), monodisperse distributions (Hassaini *et al.* 2023), and with the numerical results of Uhlmann & Chouippe (2017), who considered a monodisperse population of finite-size particles with $D/\eta = 5$. The PDFs in figure 10c and 10d exhibit a power-law behaviour spanning approximately two decades, suggesting a self-similarity in the structure of the clusters consistent with the theory of Goto & Vassilicos (2006). The power-law region sets in for volumes larger than the $\langle \mathcal{V}_{\text{cluster}} \rangle$, and features a slope close to $-16/9$ for the case $M_p = 0.1$ (blue) and to -2 for $M_p = 0.2$ (orange). For $M_p = 0.1$, the power-law region extends up to volumes $O(\mathcal{L}^3)$, \mathcal{L} being the integral scale (vertical solid lines in figure 10d). The exponent $-16/9$ was predicted by Yoshimoto & Goto (2007), who extended the fractal model of Goto & Vassilicos (2006) to the three-dimensional case. This model describes the statistical distribution of cluster areas in two-dimensional isotropic turbulence, and relies on the assumption of a fully developed inertial subrange, as well as on the correspondence between void areas and self-similar eddies at discrete scales. In the two-dimensional case, the model predicts the PDF for the cluster areas to decay with a slope $-5/3$. Sumbekova *et al.* (2017) performed wind-tunnel measurements on sub-Kolmogorov particles at $Re_\lambda \leq 400$ and reported a $-5/3$ scaling after normalising each PDF by its temporal average. Uhlmann & Chouippe (2017), who performed PR-DNS of finite-size particles with ($D/\eta = 5$), reported a slope $-16/9$, in good agreement with the theory of Yoshimoto & Goto (2007). Baker *et al.* (2017) performed point-particle DNS of smaller-than-Kolmogorov spherical particles in homogeneous isotropic turbulence, and reported a slope close to -2 for large $\mathcal{V}_{\text{cluster}}$. More recently, Hassaini *et al.* (2023) computed the PDFs of the cluster areas from particle-image-velocimetry measurements of a turbulent flow field laden with smaller-than-Kolmogorov

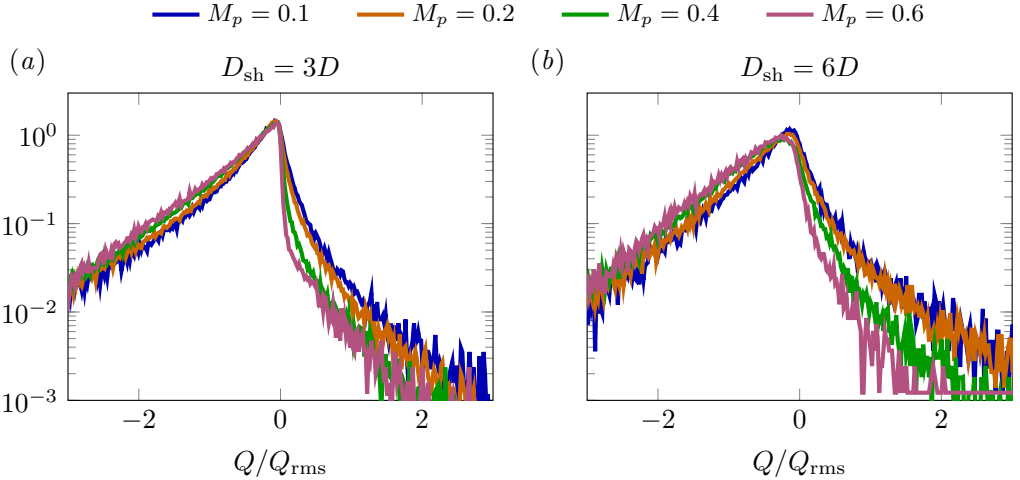


Figure 11. Probability density function (PDF) of the second invariant of the velocity gradient tensor normalised on its root-mean-square value Q/Q_{rms} , evaluated at the particle position for increasing M_p . The normalised invariant Q is evaluated within a spherical shell with an external diameter (a) $D_{\text{sh}} = 3D$ and (b) $D_{\text{sh}} = 6D$.

particles. The slope depended on the width of the field of view, but was close to -2 in all cases.

The PDFs in figure 10c and 10d do not exhibit a clear broadening of the self-similar clustering range when M_p and St_η increase, Re_λ decreases, and Φ_p is held constant. This behaviour contrasts with the experimental findings of Hassaini *et al.* (2023, see figure 3 therein), who reported a widening of the self-similar range with increasing M_p and Φ_p , while keeping Ψ_p , St_η , and Re_λ constant for monodisperse sub-Kolmogorov particles, thus suggesting a complex interaction among the various parameters governing the flow. In the present work, clustering attenuation is accompanied by a reduction of Re_λ and the departure of the energy spectra from the inertial subrange. The PDFs of $\mathcal{V}_{\text{cluster}}\eta^{-3}$ (figure 10d) show that only the very small clusters ($\mathcal{V}_{\text{cluster}}^{1/3} < 8\eta$) and the large clusters of length $\mathcal{V}_{\text{cluster}}^{1/3} > \langle \mathcal{V}_{\text{cluster}} \rangle^{1/3}$ are affected by increasing particle inertia. Comparison of figures 10b,d shows that, as Ψ_p and M_p increase, the number of particles in the smallest clusters remains constant, but their Voronoi volumes shrink, while larger clusters are populated by fewer particles.

3.7. Preferential concentration

In this section, we investigate whether the motion of heavy Kolmogorov-size particles is influenced by the centrifugal mechanism proposed by Maxey (1987). Following Squires & Eaton (1990) and Chiarini *et al.* (2025), we compute the probability density function (PDF) of the second invariant of $\partial_j u_i$ (3.7a), normalized by its root-mean-square value, Q/Q_{rms} , and evaluated in the vicinity of the particle. This local value of Q is estimated by volume averaging over a spherical shell with inner diameter D and outer diameter D_{sh} . The resulting statistics depend on the choice of D_{sh} : if the shell is too thin, the averaging primarily captures shear stresses at the particle surface; if it is too thick, spurious contributions from regions far from the particle are included (Uhlmann & Chouippe 2017; Oka & Goto 2022). The effect of varying D_{sh} was previously investigated by Chiarini *et al.* (2025) (see figure 20 therein), who showed that Kolmogorov-size spheres of moderate inertia ($\Psi_p = 5, 100$) preferentially sample regions of negative Q (i.e. where strain overcomes vorticity).

In the present work, we compute the averaged Q using $D_{\text{sh}} = 3D$ (Uhlmann & Chouippe 2017) and compare the results with those obtained using $D_{\text{sh}} = 6D$. The effect of particle inertia on the PDFs of Q/Q_{rms} is shown in figure 11a ($D_{\text{sh}} = 3D$) and 11b ($D_{\text{sh}} = 6D$) for increasing M_p . These PDFs are negatively skewed in all cases, which indicates that Kolmogorov-size particles sample strain-dominated regions and avoid vortical regions. Regardless of the value of D_{sh} , the left tail increases and the right tail decreases as M_p increases, meaning that the preferential sampling becomes more pronounced as M_p increases from 0.1 to 0.4. The case $M_p = 0.6$ (magenta curves in figure 11) shows a similar trend, but does not feature a canonical Kolmogorov cascade and thus deserves more attention. The regions of very high dissipation rate and enstrophy shown in the insets in the visualizations 1d and 2d, respectively, are located in the shear layers and in the symmetric laminar wakes that appear when the average particle Reynolds number is $\langle \text{Re}_p \rangle \gtrsim 1$ (see table 2). A possible explanation is that, as particle inertia increases, the nonlinear transfer of kinetic energy Π vanishes and the spectral balance (3.4) is mediated by the fluid-particle interaction term Π_{fs} and the dissipation D_v . The intermediate- and small-scale eddies weaken, the peaks of ε and \mathcal{E} become localised in the particles' shear layers, and clustering is no longer observed. Hence, heavy Kolmogorov-size particles sample regions of high strain and low enstrophy, but the centrifugal mechanism may affect their trajectory only in the presence of a fully-developed inertial subrange and for moderate values of Ψ_p . The strength of the centrifugal mechanism is amplified as the particle inertia increases, but vanishes along with the turbulent cascade for the largest Ψ_p and M_p .

To gain further insights on the interplay between particle clustering and preferential concentration, we compute the joint probability density function (JPDF) of the normalised Voronoi volumes $\mathcal{V}_{\text{voro}}/\langle \mathcal{V}_{\text{voro}} \rangle$ and the normalised second invariant of the velocity tensor evaluated at the particle position Q/Q_{rms} (Tagawa *et al.* 2012). The results are shown in figure 12 for (a) $M_p = 0.1$, (b) $M_p = 0.2$, (c) $M_p = 0.4$ and (d) $M_p = 0.6$. The values of $\mathcal{V}_{\text{voro}}/\langle \mathcal{V}_{\text{voro}} \rangle$ corresponding to the low and high cross-over points (LCO and HCO) are also shown as white dashed and dash-dotted lines, respectively. Once again, we computed these joint distributions by volume-averaging Q within a spherical shell of outer diameter $D_{\text{sh}} = 3D$ around the particles (Uhlmann & Chouippe 2017; Chiarini *et al.* 2025). Voronoi volumes smaller than the LCO threshold correlate with negative values of Q/Q_{rms} for the cases $M_p = 0.1$ and $M_p = 0.2$. In these cases, the LCO threshold intersects the peak of the joint distribution (red region in figures 12a,b). Thus, the particles that are most likely to be part of a cluster lie in high-strain, low-enstrophy regions of negative Q . A similar conclusion can be drawn for the case $M_p = 0.4$, although the peak of the joint distribution now lies between the HCO and LCO thresholds and the amount of the particles with $\mathcal{V}_{\text{voro}}/\langle \mathcal{V}_{\text{voro}} \rangle < \text{LCO}$ is smaller. This result is consistent with the steep decrease of the cluster characteristic length $\langle \mathcal{V}_{\text{cluster}} \rangle^{1/3}$ and the number of particles per cluster $\langle N_{\text{cluster}} \rangle$ that we observe when the mass fraction increases from 0.2 to 0.4 (see table 3). While Chiarini *et al.* (2025) showed that the joint probability of negative Q and small Voronoi volumes increases as Ψ_p increased from 5 to 100, figure 12 shows that the opposite occurs when particle inertia increases beyond $\Psi_p = 100$. The present results are in qualitative agreement with those of Tagawa *et al.* (2012, see figure 7 therein), who performed point-particle DNSs and reported the joint PDF of the normalised Voronoi volumes and enstrophy at $Re_\lambda = 75$, $St_\eta = 0.6$, and in the limits $\Psi_p \ll 1$ and $\Psi_p \gg 1$. They observed a stronger correlation between small Voronoi volumes and large enstrophy for small Ψ_p — consistent with PR-DNS results (Chiarini *et al.* 2025) — as well as enhanced clustering in the large- Ψ_p limit. The discrepancies at large Ψ_p are likely attributable to the lower Re_λ and to the inherent limitations of the point-particle approximation.

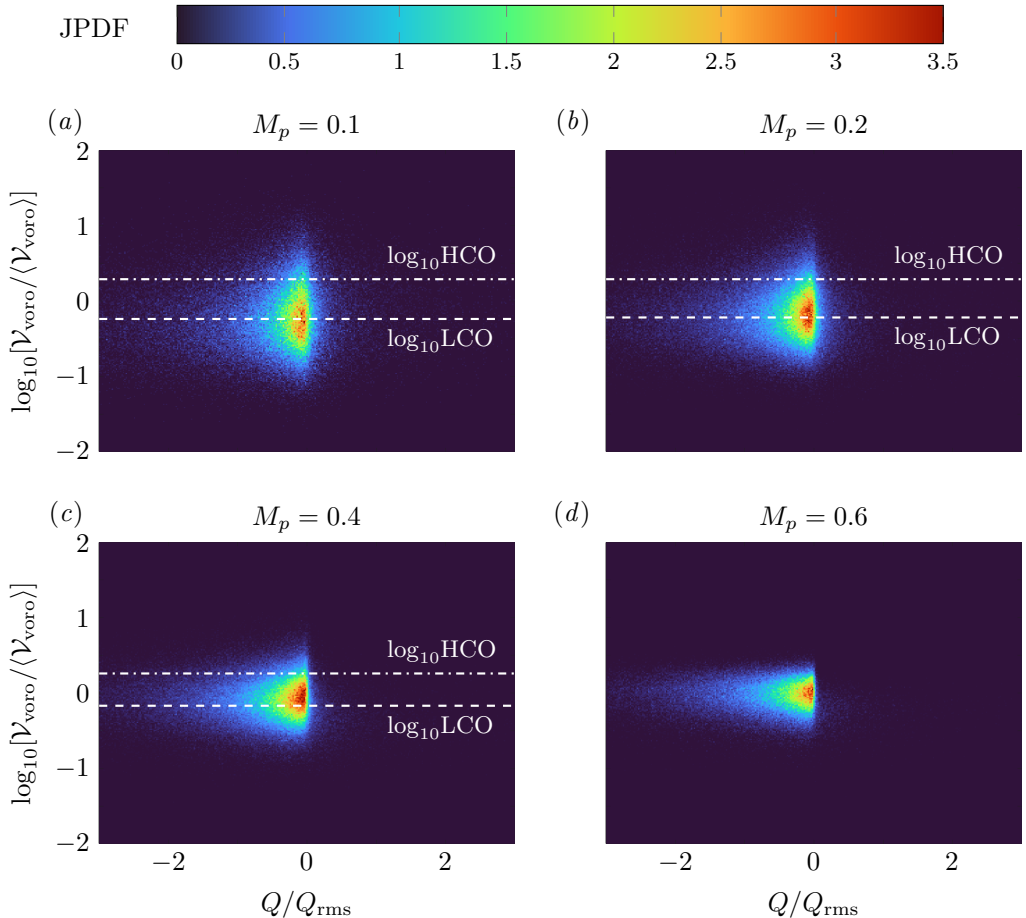


Figure 12. Joint probability density function (JPDF) of the normalised second invariant of the velocity gradient tensor Q (3.7a) evaluated around the particles, and the normalised Voronoi volume $\mathcal{V}_{\text{voro}}/\langle \mathcal{V}_{\text{voro}} \rangle$ for (a) $M_p = 0.1$, (b) $M_p = 0.2$, (c) $M_p = 0.4$ and (d) $M_p = 0.6$. The magnitude of the JPDF is described by the colorbar at the top of the four panels. The position of the high cross-over (HCO) and low cross-over (LCO) points are plotted with the white dash-dotted and white dashed lines, respectively (refer also to table 3). The second invariant Q was computed by averaging over a spherical shell of diameter $D_{\text{shell}} = 3D$ around the particle.

4. Conclusions

We investigate homogeneous and isotropic turbulence laden with a dilute suspension of heavy, Kolmogorov-scale particles. To quantify the particle-fluid feedback, we perform particle-resolved direct numerical simulations (PR-DNSs) in a triperiodic cubic domain containing a monodisperse population of 74 208 solid spheres. Fluid-solid interactions are resolved using the Eulerian immersed boundary method (IBM) of Hori *et al.* (2022). The particle diameter, domain size, and fluid properties are held fixed to isolate the effects of increasing particle-to-fluid density ratio and mass fraction at constant volume fraction $\Phi_p = 10^{-3}$. Four density ratios are considered, $\Psi_p = 100, 250, 666$, and 1499 , corresponding to mass fractions $M_p = 0.1, 0.2, 0.4$, and 0.6 , respectively. In the unladen reference case, a Taylor-scale Reynolds number $Re_\lambda \simeq 150$ is achieved, ensuring adequate scale separation and the presence of an inertial subrange extending over around one decade of wavenumbers.

The bulk properties of the carrier flow are substantially modified once the particle-to-fluid density ratio exceeds $\Psi_p = 100$. As particle inertia increases, the dispersed phase extracts a significant amount of the kinetic energy from the carrier flow, leading to a marked reduction of the Taylor-scale Reynolds number. The bulk dissipation rate is also affected. However, the Kolmogorov length scale remains approximately constant and comparable to the particle diameter across all cases. The energy spectra exhibit a progressive departure from the classical Kolmogorov $\kappa^{-5/3}$ scaling as the mass fraction increases. When the flow is laden, the spectra display a κ^{-4} decay at high wavenumbers, corresponding to sub-Kolmogorov and sub-particle scales. This scaling is reminiscent of those reported in bubbly flows and has recently been observed in particle-resolved simulations by Chiarini *et al.* (2025). At low and intermediate wavenumbers, the classical Kolmogorov scaling is replaced by a κ^{-1} regime when the flow is laden with the heaviest particles. This behaviour is consistent with the anomalous scaling of the second-order structure function, which follows $S_2 \sim \log(r/\eta)$ for separations larger than the particle diameter, and indicates a loss of velocity correlations (Olivieri *et al.* 2022a). Further insight into the flow modulation is obtained from the scale-by-scale energy budget (Pope 2000). As the mass loading increases, the nonlinear energy transfer term weakens, while the fluid-solid interaction term becomes increasingly dominant. In the case of the heaviest particles, the energy balance is controlled primarily by the mechanical work of the fluid-solid interaction and by viscous dissipation across the whole spectrum, whereas the nonlinear interactions that characterise the classical Kolmogorov cascade are fully suppressed. Finally, the local structure of the flow is examined through the invariants Q and R of the velocity gradient tensor $\partial u_i / \partial x_j$ (Meneveau 2011). Increasing particle inertia enhances strain-dominated events at the expense of enstrophy, leading to a balance between axial and biaxial strain and between vortex stretching and compression. Consistently, the joint probability density functions of Q and R exhibit an increased probability along the negative- R branch of the Vieillefosse tail.

We investigate the collective motion of the particles by computing their velocity PDFs and the mean square displacement (MSD). The average and the standard deviation of the absolute velocity decrease, while the average particle Reynolds number – which is defined on the relative velocity of the particle and the fluid – increases slightly with the density ratio. The MSD shows a ballistic behavior for short times and approaches the Brownian limit for larger times with the progressively more time needed for this transition, as the inertia grows. We characterise the degree of clustering and the structure of the clusters using the Voronoi tessellation (Monchaux *et al.* 2010). The PDFs of the Voronoi volumes are broader for $\Psi_p = 100$ and collapse on the PDF of a random Poisson process as the density ratio increases. The standard deviation of the volumes, which quantifies the degree of clustering, decreases for $\Psi_p > 100$. Our results are complementary to those of Chiarini *et al.* (2025), who reported an intensification of clustering when the density ratio increased from $\Psi_p = 5$ to 100 for a suspension of Kolmogorov-size particles of equal volume fraction. No clusters can be identified in the heaviest-particle case, for which the PDF of the volumes collapses on that of the RPP. The PDFs of the cluster volumes show a power-law decay close to the exponents $-16/9$ and -2 . The first is consistent with the fractal model of Yoshimoto & Goto (2007) and the second has been reported in numerical and experimental works (Baker *et al.* 2017; Hassaini *et al.* 2023). The clusters shrink and become less and less populated as the density ratio increases. When computed near the particle surface, the PDFs of the invariant Q are negatively skewed, meaning that heavy Kolmogorov-size particles sample regions where strain prevails over vorticity. The joint PDFs of Q and the Voronoi volumes show that the small volumes correlate with negative Q , thus suggesting that the preferential sampling fosters cluster formation.

Future work should address the role of multidisperse (i.e. non-uniform) suspensions of spherical and non-spherical Kolmogorov-size particles. In addition, further particle image velocimetry measurements with sub-Kolmogorov resolution (Tanaka & Eaton 2010) are needed to resolve the multiscale structure of flows laden with Kolmogorov-size particles.

Acknowledgements The authors acknowledge the computational resources provided by the Scientific Computing & Data Analysis Section of the Core Facilities at OIST and by HPCI under Research Project grants hp230536, hp250021, and hp250035.

Funding The research was supported by the Okinawa Institute of Science and Technology Graduate University (OIST) with subsidy funding to M.E.R. from the Cabinet Office, Government of Japan. M.E.R. also acknowledges funding from the Japan Society for the Promotion of Science (JSPS), grant 24K17210 and 24K00810.

Declaration of interests The authors report no conflict of interest.

Author ORCIDs

L. Fossà, <https://orcid.org/0000-0001-7138-5903>

M. E. Rosti, <https://orcid.org/0000-0002-9004-2292>

REFERENCES

AMSDEN, A. A. & HARLOW, F. H. 1970 A simplified MAC technique for incompressible fluid flow calculations. *J. Comput. Phys.* **6** (2), 322–325.

ARDEKANI, M. N. & BRANDT, L. 2019 Turbulence modulation in channel flow of finite-size spheroidal particles. *J. Fluid Mech.* **859**, 887–901.

ARNOLD, V. I. 1965 Sur la topologie des écoulements stationnaires des fluides parfaits. *C. R. Acad. Sci. Paris* **261**, 17–20.

BAKER, L., FRANKEL, A., MANI, A. & COLETTI, F. 2017 Coherent clusters of inertial particles in homogeneous turbulence. *J. Fluid Mech.* **833**, 364–398.

BALACHANDAR, S. & EATON, J. K. 2010 Turbulent dispersed multiphase flow. *Ann. Rev. Fluid Mech.* **42** (Vol. 42, 2010), 111–133.

BALACHANDAR, S., LIU, K. & LAKHOTE, M. 2019 Self-induced velocity correction for improved drag estimation in Euler–Lagrange point-particle simulations. *J. Computat. Phys.* **376**, 160–185.

BENZI, R., CILIBERTO, S., TRIPICCIONE, R., BAUDET, C., MASSAIOLI, F. & SUCCI, S. 1993 Extended self-similarity in turbulent flows. *Phys. Rev. E* **48**, R29–R32.

BETCHOV, R. 1956 An inequality concerning the production of vorticity in isotropic turbulence. *J. Fluid Mech.* **1** (5), 497–504.

BIRNSTIEL, T. 2024 Dust growth and evolution in protoplanetary disks. *Ann. Rev. Astron. Astrophys.* **62** (Vol. 62, 2024), 157–202.

BORGNINO, M., ARRIETA, J., BOFFETTA, G., DE LILLO, F. & TUVAL, I. 2019 Turbulence induces clustering and segregation of non-motile, buoyancy-regulating phytoplankton. *J. Royal Soc. Interface* **16** (159), 20190324.

BRANDT, L. & COLETTI, F. 2022 Particle-laden turbulence: Progress and perspectives. *Ann. Rev. Fluid Mech.* **54** (Vol. 54, 2022), 159–189.

BREUGEM, W.-P. 2012 A second-order accurate immersed boundary method for fully resolved simulations of particle-laden flows. *J. Comput. Phys.* **231** (13), 4469–4498.

CANNON, I., OLIVIERI, S. & ROSTI, M. E. 2024 Spheres and fibers in turbulent flows at various Reynolds numbers. *Phys. Rev. Fluids* **9**, 064301.

CANTWELL, B. J. 1992 Exact solution of a restricted Euler equation for the velocity gradient tensor. *Phys. Fluids A: Fluid Dyn.* **4** (4), 782–793.

CHIARINI, A., CANNON, I. & ROSTI, M. E. 2024 Anisotropic mean flow enhancement and anomalous transport of finite-size spherical particles in turbulent flows. *Phys. Rev. Lett.* **132**, 054005.

CHIARINI, A. & ROSTI, M. E. 2024 Finite-size inertial spherical particles in turbulence. *J. Fluid Mech.* **988**, A17.

CHIARINI, A., TANDURELLA, S. & ROSTI, M. E. 2025 Kolmogorov-size particles in homogeneous and isotropic turbulence. *J. Fluid Mech.* **1007**, A81.

CHOUIPPE, A. & UHLMANN, M. 2019 On the influence of forced homogeneous-isotropic turbulence on the settling and clustering of finite-size particles. *Acta Mech.* **230** (2), 387–412.

CODISPOTI, L. A., MEYER, D. W. & JENNY, P. 2025 Dissecting inertial clustering and sling dynamics in high-Reynolds number particle-laden turbulence. *Phys. Fluids* **37** (1), 015161.

COSTA, P., BOERSMA, B. J., WESTERWEEL, J. & BREUGEM, W.-P. 2015 Collision model for fully resolved simulations of flows laden with finite-size particles. *Phys. Rev. E* **92**, 053012.

COSTA, P., BRANDT, L. & PICANO, F. 2021 Near-wall turbulence modulation by small inertial particles. *J. Fluid Mech.* **922**, A9.

DAVIDSON, P. 2015 *Turbulence: An Introduction for Scientists and Engineers*. Oxford University Press.

FIABANE, L., ZIMMERMANN, R., VOLK, R., PINTON, J.-F. & BOURGOIN, M. 2012 Clustering of finite-size particles in turbulence. *Phys. Rev. E* **86**, 035301.

FREUND, J. B. 2014 Numerical simulation of flowing blood cells. *Ann. Rev. Fluid Mech.* **46** (Volume 46, 2014), 67–95.

GAO, W., SAMTANEY, R. & RICHTER, D. H. 2023 Direct numerical simulation of particle-laden flow in an open channel at $re_\tau = 5186$. *J. Fluid Mech.* **957**, A3.

GORE, R.A. & CROWE, C.T. 1989 Effect of particle size on modulating turbulent intensity. *Int. J. Multiph. Flow* **15** (2), 279–285.

GOTO, S. & VASSILICOS, J. C. 2006 Self-similar clustering of inertial particles and zero-acceleration points in fully developed two-dimensional turbulence. *Phys. Fluids* **18** (11), 115103.

GOTO, S. & VASSILICOS, J. C. 2008 Sweep-stick mechanism of heavy particle clustering in fluid turbulence. *Phys. Rev. Lett.* **100**, 054503.

GUALTIERI, P., BATTISTA, F., SALVADORE, F. & CASCIO, C.M. 2023 Effect of Stokes number and particle-to-fluid density ratio on turbulence modification in channel flows. *J. Fluid Mech.* **974**, A26.

HASSAINI, R., PETERSEN, A. J. & COLETTI, F. 2023 Effect of two-way coupling on clustering and settling of heavy particles in homogeneous turbulence. *J. Fluid Mech.* **976**, A12.

HORI, N., ROSTI, M. E. & TAKAGI, S. 2022 An Eulerian-based immersed boundary method for particle suspensions with implicit lubrication model. *Comput. Fluids* **236**, 105278.

HWANG, W. & EATON, J. K. 2006 Homogeneous and isotropic turbulence modulation by small heavy ($St \sim 50$) particles. *J. Fluid Mech.* **564**, 361–393.

JENNY, P., ROEKAERTS, D. & BEISHUIZEN, N. 2012 Modeling of turbulent dilute spray combustion. *Prog. Energy Combust. Sci.* **38** (6), 846–887.

KAJISHIMA, T., TAKIGUCHI, S., HAMASAKI, H. & MIYAKE, Y. 2001 Turbulence structure of particle-laden flow in a vertical plane channel due to vortex shedding. *JSME Int. J. Ser. B Fluids Therm. Eng.* **44** (4), 526–535.

KEMPE, T. & FRÖHLICH, J. 2012 An improved immersed boundary method with direct forcing for the simulation of particle laden flows. *J. Comput. Phys.* **231** (9), 3663–3684.

KIM, J., MOIN, P. & MOSER, R. 1987 Turbulence statistics in fully developed channel flow at low Reynolds number. *J. Fluid Mech.* **177**, 133–166.

LEE, B.-K., B. RAJ MOHAN, B., BYEON, S.-H., LIM, K.-S. & HONG, E.-P. 2013 Evaluating the performance of a turbulent wet scrubber for scrubbing particulate matter. *J. Air Waste Manag. Assoc.* **63** (5), 499–506.

LU, J., LAZAR, E. A. & RYCROFT, C. H. 2023 An extension to Voro++ for multithreaded computation of Voronoi cells. *Comput. Phys. Commun.* **291**, 108832.

LUCCI, F., FERRANTE, A. & ELGHOBASHI, S. 2010 Modulation of isotropic turbulence by particles of taylor length-scale size. *J. Fluid Mech.* **650**, 5–55.

LUO, K., WANG, Z., LI, D., TAN, J. & FAN, J. 2017 Fully resolved simulations of turbulence modulation by high-inertia particles in an isotropic turbulent flow. *Phys. Fluids* **29** (11), 113301.

MARCHIOLI, C., BOURGOIN, M., COLETTI, F., FOX, R. O., MAGNAUDET, J., REEKS, M., SIMONIN, O., SOMMERFELD, M., TOSCHI, F., WANG, L.-P. & BALACHANDAR, S. 2025 Particle-laden flows. *Int. J. Multiph. Flow* **191**, 105291.

MARCHIOLI, C., ROSTI, M. E. & VERHILLE, G. 2026 Flexible fibers in turbulence. *Ann. Rev. Fluid Mech.* **58** (Volume 58, 2026), 167–192.

MATSUDA, K., YOSHIMATSU, K. & SCHNEIDER, K. 2024 Heavy particle clustering in inertial subrange of high-Reynolds number turbulence. *Phys. Rev. Lett.* **132**, 234001.

MAXEY, M. R. 1987 The gravitational settling of aerosol particles in homogeneous turbulence and random flow fields. *J. Fluid Mech.* **174**, 441–465.

MAXEY, M. R. & RILEY, J. J. 1983 Equation of motion for a small rigid sphere in a nonuniform flow. *Phys. Fluids* **26** (4), 883–889.

MELLADO, J. P. 2017 Cloud-top entrainment in stratocumulus clouds. *Ann. Rev. Fluid Mech.* **49** (Volume 49, 2017), 145–169.

MENEVEAU, C. 2011 Lagrangian dynamics and models of the velocity gradient tensor in turbulent flows. *Ann. Rev. Fluid Mech.* **43** (Vol. 43, 2011), 219–245.

MONCHAUX, R. 2012 Measuring concentration with Voronoi diagrams: the study of possible biases. *New J. Phys.* **14** (9), 095013.

MONCHAUX, R., BOURGOIN, M. & CARTELLIER, A. 2010 Preferential concentration of heavy particles: A Voronoï analysis. *Phys. Fluids* **22** (10), 103304.

MONTI, A., RATHEE, V., SHEN, A. Q. & ROSTI, M. E. 2021 A fast and efficient tool to study the rheology of dense suspensions. *Phys. Fluids* **33** (10), 103314.

MORTIMER, L. F. & FAIRWEATHER, M. 2020 Density ratio effects on the topology of coherent turbulent structures in two-way coupled particle-laden channel flows. *Phys. Fluids* **32** (10), 103302.

OBLIGADO, M., TEITELBAUM, T., CARTELLIER, A., MININNI, P. & BOURGOIN, M. 2014 Preferential concentration of heavy particles in turbulence. *J. Turbul.* **15** (5), 293–310.

OKA, S. & GOTO, S. 2022 Attenuation of turbulence in a periodic cube by finite-size spherical solid particles. *J. Fluid Mech.* **949**, A45.

OLIVIERI, S., CANNON, I. & ROSTI, M. E. 2022a The effect of particle anisotropy on the modulation of turbulent flows. *J. Fluid Mech.* **950**, R2.

OLIVIERI, S., MAZZINO, A. & ROSTI, M. E. 2022b On the fully coupled dynamics of flexible fibres dispersed in modulated turbulence. *J. Fluid Mech.* **946**, A34.

PoELMA, C., WESTERWEEL, J. & OOMS, G. 2007 Particle–fluid interactions in grid-generated turbulence. *J. Fluid Mech.* **589**, 315–351.

POPE, S.B. 2000 *Turbulent Flows*. Cambridge University Press.

PRAKASH, V. N., MARTÍNEZ MERCADO, J., VAN WIJNGAARDEN, L., MANCILLA, E., TAGAWA, Y., LOHSE, D. & SUN, C. 2016 Energy spectra in turbulent bubbly flows. *J. Fluid Mech.* **791**, 174–190.

RAMIREZ, G., BURLOT, A., ZAMANSKY, R., BOIS, G. & RISSO, F. 2024 Spectral analysis of dispersed multiphase flows in the presence of fluid interfaces. *Int. J. Multiph. Flow* **177**, 104860.

ROSE, W. I. & DURANT, A. J. 2009 Fine ash content of explosive eruptions. *J. Volcanol. Geotherm. Res.* **186** (1), 32–39.

ROSTAMI, A., LI, R. & KHEIRKHAH, S. 2024 Three-dimensional clustering characteristics of large-Stokes-number dilute sprays interacting with turbulent swirling co-flows. *J. Fluid Mech.* **999**, A73.

ROSTI, M. E. & BRANDT, L. 2020 Increase of turbulent drag by polymers in particle suspensions. *Phys. Rev. Fluids* **5**, 041301.

SCHNEIDERS, L., MEINKE, M. & SCHRÖDER, W. 2017 Direct particle–fluid simulation of Kolmogorov-length-scale size particles in decaying isotropic turbulence. *J. Fluid Mech.* **819**, 188–227.

SHEN, J., PENG, C., LU, Z. & WANG, L.-P. 2024 The influence of particle density and diameter on the interactions between the finite-size particles and the turbulent channel flow. *Int. J. Multiph. Flow* **170**, 104659.

SQUIRES, K. D. & EATON, J. K. 1990 Particle response and turbulence modification in isotropic turbulence. *Phys. Fluids A: Fluid Dyn.* **2** (7), 1191–1203.

SUGATHAPALA, T. M., CAPUANO, T., BRANDT, L., IUDICONE, D. & SARDINA, G. 2025 Vertical transport of buoyant microplastic particles in the ocean: The role of turbulence and biofouling. *Environ. Pollut.* **369**, 125819.

SUMBKOVA, S., CARTELLIER, A., ALISEDA, A. & BOURGOIN, M. 2017 Preferential concentration of inertial sub-Kolmogorov particles: The roles of mass loading of particles, Stokes numbers, and Reynolds numbers. *Phys. Rev. Fluids* **2**, 024302.

TAGAWA, Y., MERCADO, J. M., PRAKASH, VIVEK N., CALZAVARINI, E., SUN, C. & LOHSE, D. 2012 Three-dimensional Lagrangian Voronoï analysis for clustering of particles and bubbles in turbulence. *J. Fluid Mech.* **693**, 201–215.

TANAKA, T. & EATON, J. K. 2010 Sub-Kolmogorov resolution particle image velocimetry measurements of particle-laden forced turbulence. *J. Fluid Mech.* **643**, 177–206.

TAVANASHAD, V., PASSALACQUA, A., FOX, R. O. & SUBRAMANIAM, S. 2019 Effect of density ratio on velocity fluctuations in dispersed multiphase flow from simulations of finite-size particles. *Acta Mech.* **230** (2), 469–484.

TOMÉ, M. F., DUFFY, B. & MCKEE, S. 1996 A numerical technique for solving unsteady non-Newtonian free surface flows. *J. Non-Newton. Fluid Mech.* **62** (1), 9–34.

TSUJI, Y., KAWAGUCHI, T. & TANAKA, T. 1993 Discrete particle simulation of two-dimensional fluidized bed. *Powder Tech.* **77** (1), 79–87.

UHLMANN, M. 2005 An immersed boundary method with direct forcing for the simulation of particulate flows. *J. Comput. Phys.* **209** (2), 448–476.

UHLMANN, M. 2008 Interface-resolved direct numerical simulation of vertical particulate channel flow in the turbulent regime. *Phys. Fluids* **20** (5), 053305.

UHLMANN, M. & CHOUIPPE, A. 2017 Clustering and preferential concentration of finite-size particles in forced homogeneous-isotropic turbulence. *J. Fluid Mech.* **812**, 991–1023.

YOSHIMOTO, H. & GOTO, S. 2007 Self-similar clustering of inertial particles in homogeneous turbulence. *J. Fluid Mech.* **577**, 275–286.

YU, Z., LIN, Z., SHAO, X. & WANG, L.-P. 2017 Effects of particle-fluid density ratio on the interactions between the turbulent channel flow and finite-size particles. *Phys. Rev. E* **96**, 033102.